


2019

Expansion of an Ultracold Neutral Plasma

Yin Li

Follow this and additional works at: <https://digitalcommons.colby.edu/honorstheses>

 Part of the [Atomic, Molecular and Optical Physics Commons](#)

Colby College theses are protected by copyright. They may be viewed or downloaded from this site for the purposes of research and scholarship. Reproduction or distribution for commercial purposes is prohibited without written permission of the author.

Recommended Citation

Li, Yin, "Expansion of an Ultracold Neutral Plasma" (2019). *Honors Theses*. Paper 1357.
<https://digitalcommons.colby.edu/honorstheses/1357>

This Honors Thesis (Open Access) is brought to you for free and open access by the Student Research at Digital Commons @ Colby. It has been accepted for inclusion in Honors Theses by an authorized administrator of Digital Commons @ Colby.

Expansion of an Ultracold Neutral Plasma

An Honours Thesis

submitted in partial fulfillment of the requirements for the degree of
Bachelor of Arts with Honors in Physics

presented to
the Department of Physics
Colby College
Duncan A. Tate, Supervisor

by
Yin Li

May 21, 2019

Acknowledgements

First and foremost, I would like to express my gratitude to Professor Duncan Tate for his support throughout my four years at Colby. Without his help during the summer of 2016, I would have never entered the field of experimental atomic physics, and thanks to Professor Tate's consistent assistance, I could complete an honor degree and finish this honors thesis about expansion of ultracold neutral plasma.

I would also like to thank Colby College Physics department for their inspiring ideas and professional teaching which contributed a great part to my education in Colby College. This thesis cannot be completed without the help of Professor Conover, Professor Bluhm, Professor Kocevski, Professor McCoy, Professor McGrath and Professor Lessard.

I would like to acknowledge my parents, Ying Zhang and Quanzeng Li, for their support in my pursuing in higher degree in Physics. My girlfriend, Xiaoou (Alice) Wang always provides help during the darkest period of my physics career. Professor Maxwell in the CS department encouraged me a lot for including computational materials in this honors thesis and Professor Goodsell of Middlebury College helped me understand how to do experiments with cold atoms.

Abstract

Ultracold neutral plasmas (UNP) exhibit interesting behavior and are more feasible to control than hot plasmas. Physicists would like to lower the temperature of a UNP to achieve a higher Coulomb coupling parameter, Γ for both electrons and ions. However, the three body recombination (TBR) between ions and electrons produces Rydberg atoms and heats up the plasma electrons, thereby ionizing them to $\Gamma_e < 0.2$. Adding Rydberg atoms to the plasma will reduce the temperature of a UNP in certain situations.

In this honors project, we tried to achieve a Γ_e value greater than 0.5 by embedding Rydberg atoms multiple times in the plasma. We did extensive numerical simulations, but we were unable to replicate previous results from another group which obtained $\Gamma_e = 0.5$ in the first $1 \mu\text{ s}$ of plasma evolution. However, we were able to use the simulation results to test various different experiment scenarios. For experiments, we created a UNP of Rubidium atoms in the magneto-optical trap by laser cooling and photoionization. We figured out a nice way to zero the electric field within the field meshes by looking at the plasma expansion very late in its evolution through the micro-channel plate. We set the voltage and delay on the field mesh bias to find expansion velocity of the plasma for time $t > 50 \mu\text{s}$, and we used different methods to deduce the expansion velocity from the ion time of flight signals. However, we found that there was no relation of Γ_e at $1 \mu\text{ s}$ and the expansion velocity at a later stage of plasma evolution by simulation. To get around this, we figured out a new way to get the ions distribution at a specific time after the plasma creation by pushing all the ions to the micro-channel plate.

Contents

Acknowledgements	ii
Abstract	iii
Contents	iv
1 Introduction	1
1.1 Plasma	1
1.2 Ultracold Neutral Plasma	2
1.2.1 Creation of the UNP	3
1.2.2 Expansion of the UNP	5
1.3 Rydberg Atoms	6
1.4 Numerical Simulation	7
2 Experiment	9
2.1 Apparatus	9
2.1.1 Magneto-Optical Trap	10
2.1.2 Laser Cooling	10
2.1.3 Photo Ionization and Excitation to Rydberg States	11
2.1.4 Detection of UNP	12
2.1.5 Laser and Detection Synchronization	14
2.2 Procedure of Operation	14
3 Numerical Simulation	16
3.1 Hanson/Robicheaux program	16
3.2 Simulation Process	18
3.2.1 Adding Rydberg Atoms twice	18
3.2.2 Delaying the Addition of Rydberg atoms	18
4 Results	20
4.1 Simulation Data - 1	20

4.2	Experimental Data - 1	21
4.3	Simulation Data - 2	22
4.4	Experimental Data - 2	23
5	Discussion	25
5.1	Can we reach $\Gamma_e = 0.5$ at time $1 \mu s$ plasma evolution time by simulation? .	25
5.2	Can we infer Γ_e at $1 \mu s$ from the plasma expansion velocity by both simulation and experiment?	25
6	Conclusion and Future Work	27
A	Computer Science Capstone Experience	28
B	Physical Review A Paper	31
	Bibliography	45

1. Introduction

1.1 Plasma

Plasma, or the ionized gas [2], is one of the four fundamental states of matter, the other three being our familiar gas, solid, and water. Though abundant in the universe, plasma is not so common on Earth compared with the other three due to the temperature. Plasma can be generated by heating a neutral gas to the point where ionization occurs at high enough charge density that a quasi-stable configuration arises [10]. Just like the thermal motion of atoms breaks the crystal structure to form a liquid, overcomes the speed of recondensation to form a gas, when the atoms are heated enough, the thermal motion of the atoms is able to knock off their electrons so that the flow of the ions and electrons form electric and magnetic fields. The name, “plasma”, comes from the Nobel Prize laureate Irving Langmuir and it means “moldable substance” in Greek and indeed the mercury arc plasma he worked with tended to diffuse throughout the glass chamber, filling it like a jelly in a mold.[10]

Though not prominent, plasma is everywhere in our life, including TV screens, rocket exhausts, lightning and the aurora. Research on plasmas also shines light on many dominant fields. For example, X-ray lasers depend on collisional excitation of more energetic states of partially ionized atoms in a plasma [2]. The study of plasma is also important in nuclear physics where physicists would like to understand the behavior of the plasmas produced after a nuclear reaction to further control the reaction itself. Moreover, the field of plasma chemistry studies the chemical reactions in plasmas where the reactions are made possible by the highly excited states in plasmas. Plasmas are also used in surface processing in the semiconductor industry. [2]

There are two major characteristics of a plasma: its temperature (K) and its number density (charged particles/m³). Plasmas tend to be very hot because the energy required to break a neutral atom into ions and electrons is of the magnitude of an electron volt (i.e. 10⁴ K). Plasmas with electron temperature lower than 1 eV cannot be self-sustaining. Given the enormous temperature to create a plasma and the low self-sustainability, research on plasmas generally requires very special apparatus. The problem is that a container cannot be as hot as the plasma to remain in the solid state. Typically, the plasma needs to be

created by short electric pulse so that the container can be cooled between the experiments. On the other hand, physicists asked the question that whether it would be possible to extend the limit of the plasma to temperatures lower than the room temperature even as low as several Kelvin where experiments will be more feasible. This led to the discovery of ultracold neutral plasma in 1999.

1.2 Ultracold Neutral Plasma

Though we typically think plasma only exists in high temperature with rapid thermal motions of ions and electrons, it turns out that we can create plasma in a low temperature and so physicists called them ultracold neutral plasma (UNP). Figure 1.1 shows the position of the UNP in the spectrum of plasma environment. The study of ultracold neutral plasmas helps improve the understanding of strongly interacting many-body system. Surprisingly, the properties of UNPs can be related to those energetic plasmas including the interior of white dwarf [6].

A key parameter for both an ultracold neutral plasma and a general plasma is its Coulomb coupling parameter defined as

$$\Gamma = \frac{E_{interaction}}{E_{thermal}} = \frac{e^2}{4\pi\epsilon_0 a} \frac{1}{k_B T} \quad (1.1)$$

where $a = (3/4\pi n)^{1/3}$ is the inter-particle spacing and n is the plasma number density. Notice that here the temperature can be different for electrons and ions, so we have different values for Γ_e and Γ_i . In Figure 1.1, the red line refers to the value of $\Gamma = 1$ and the closer to lower right corner represents a higher Γ value.

Typically, the lower the temperature and the higher the number density, the higher Coulomb coupling parameter Γ is for the plasma. In conventional hot plasmas, the thermal energy dominates the total energy, so $\Gamma \ll 1$, which means that the atoms can hardly feel the interaction between them. In some extreme conditions like the crust of a neutron star where the density is extremely high (10^{17} kg/m³), the Coulomb coupling parameter can be larger than 1. We called such a system a "strongly coupled plasma". Plasmas with different Γ values behave differently. Plasma with $1 < \Gamma < 170$ shows liquid-like short range spatial correlations, and plasma with $\Gamma > 170$ performs like a solid with long range order as in a lattice[5]. Γ is able to characterize many features of a plasma and plasmas with

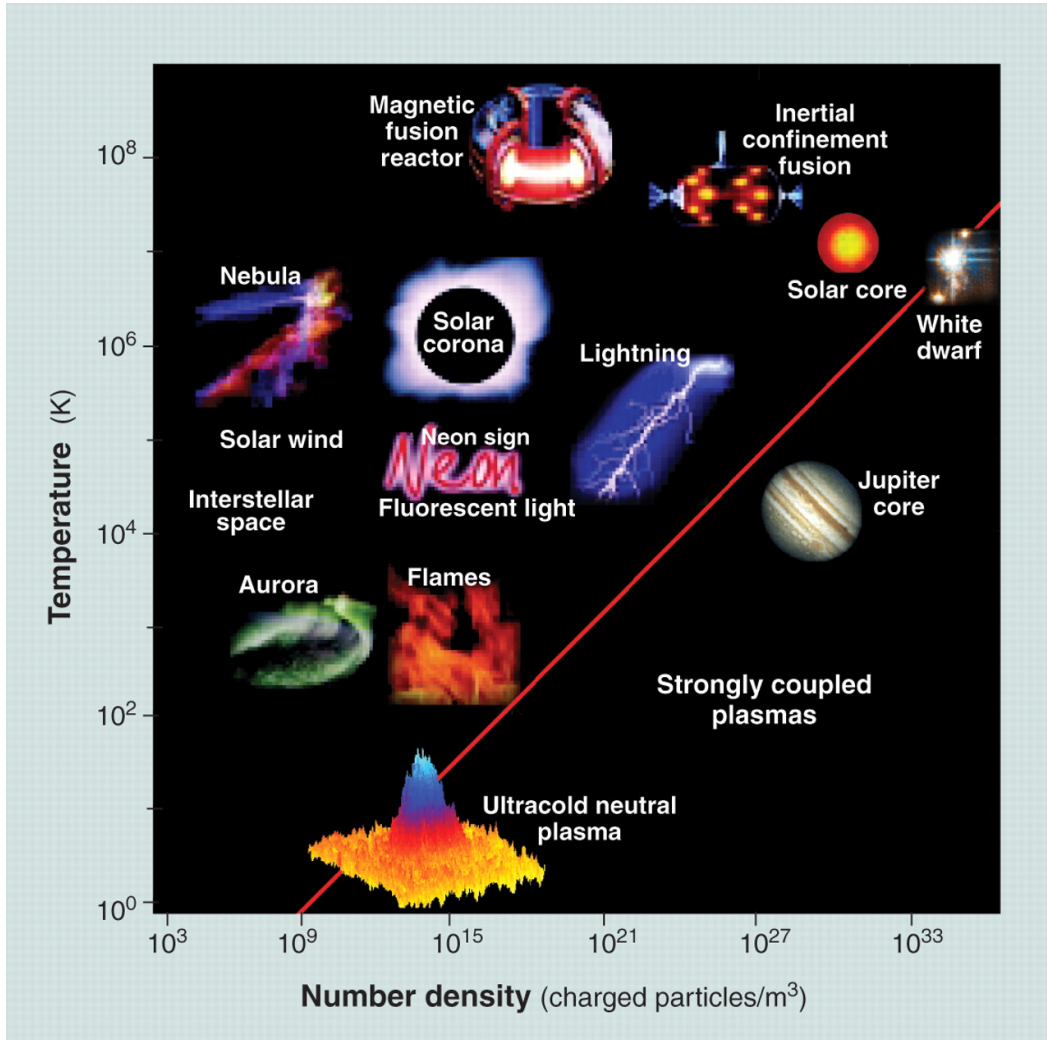


Figure 1.1: Plasma spectrum of natural and laboratory plasmas. Typically, plasmas around 1,000K are considered as cold plasmas and those around 1K are considered ultracold plasmas. Red line represents Coulomb parameter of 1 and the closer to the lower right corner, the higher the Γ value.[6]

high Γ values are especially worth doing research because the strongly coupled plasmas exhibits liquid-like or solid-like behavior. Looking at the ultracold neutral plasma is one perspective for increasing the Coulomb coupling parameter because the UNP has such a low temperature.

1.2.1 Creation of the UNP

To create an ultracold neutral plasma, physicists start by laser-cooling neutral atoms, which is the topic of Nobel Prize in 1997 [12]. Laser cooling is a specific technique physicists used to slow down the atoms by shining lasers in all six directions of the atoms' possible motions

and thus lower this temperature. Figure 1.2 gives a brief illustration of the laser cooling technique in a magneto-optical trap (MOT). More details about our laser cooling technique are discussed in Chapter 2, and the reader is more than welcome to read more about laser cooling in reference [1]. The first creation of an ultracold neutral plasma is by the group of T. C. Killian in 1999 using laser-cooled xenon atoms. They reached an electron density of $2 \times 10^9 \text{ cm}^{-3}$ and the temperatures of the electrons and ions are respectively as low as 100 mK and $10 \text{ } \mu\text{K}$ respectively. [7]

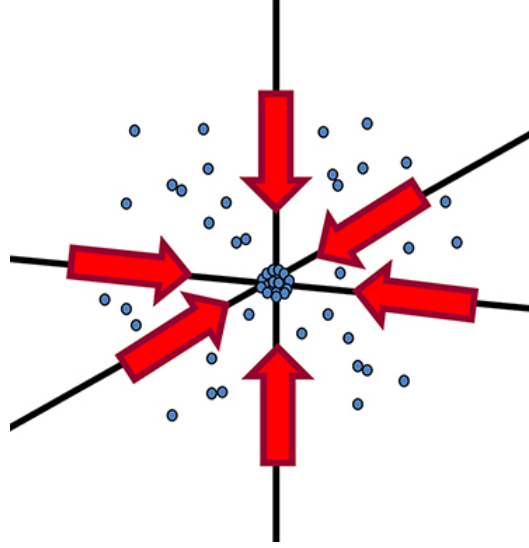


Figure 1.2: Laser cooling technique. By shining lasers in all six directions of the atoms possible motions, atoms will be slowed down by absorbing and re-emitting photons. Following that, the temperature of the atoms will be lowered.[6]

The plasma formation process is easy to understand. The cooled neutral atoms are ionized by a laser pulse of $\approx 10\text{ns}$ duration, and for Rubidium atoms, the laser wavelength will be $< 480 \text{ nm}$. Subsequently, some electrons escape the cloud of atoms, leaving the cloud slightly positively charged. As more electrons leave the plasma, it becomes harder for more electrons to escape, and the system comes to an equilibrium point. Though not created by the thermal ionization of the atoms, the plasma is dense enough to shield out the external electric fields and almost neutral with only a few percent of electrons escaped. [18]

Since strongly-coupled plasmas are especially interesting, physicists aim for reaching a strongly-coupled ultracold neutral plasma as well. However, it is not as easy as decreasing the temperature and increasing the number density. Murillo's group found out that the disorder-induced heating would severely increase the effective temperature of the ions and decrease their Coulomb coupling parameter. Murillo reported that "the rapid ion heating

occurs as correlations develop from the initial disordered configuration." [11] Additionally, three-body recombination (TBR) heats the electrons in the plasma, limiting the Coulomb coupling parameter of the electron to $\Gamma_e \approx 0.1$ [16].

1.2.2 Expansion of the UNP

The manner in which the UNP expands is unusual from the other states of matter. The first group measuring the expansion of a UNP was in 2000 [8]. Kulin discovered that in low Γ region, the expansion of the plasma is dominated by the pressure of the electron gas and is described by the hydrodynamic model. However, as Γ_e increases, there is the effect of three-body recombination, where two electrons and one ion collide to form a Rydberg atom (i.e. an atom with an electron of a very high principal quantum number). The three-body recombination is a heating process for electrons in competition against the adiabatic cooling of electrons as the plasma expands. The three body recombination rate is proportional to $n_i n_e^2 T_e^{-9/2}$. Notice that to get a high Γ_e from Equation 1.1, we need a higher n_e and a lower T_e , which correspond to a higher **heating** rate of the three body recombination.

It is possible to reverse the TBR process by embedding Rydberg atoms in the plasma because the collisional ionization of Rydberg atoms is the reverse process of the three body recombination.

The asymptotic expansion velocity of the UNP is a manifestation of the outward pressure due to the electron thermal kinetic energy, and it can be used to characterize the effective initial electron temperature in the plasma. The number density of ions in a UNP is gaussian and can be described by

$$n_i(r, t) = \frac{N_i}{(2\pi\sigma^2)^{3/2}} e^{-r^2/2\sigma^2} \quad (1.2)$$

where σ is the standard deviation of the Gaussian distribution and it is assumed that the expansion of a UNP is approximately uniform and so $\sigma = \sqrt{\sigma_0^2 + v_0^2 t^2}$, where v_0 is the plasma expansion velocity. v_0 is related to the initial ion and electron temperature by

$$v_0 = \sqrt{\frac{k_B(T_{e,0} + T_{\text{ion},0})}{m_{\text{ion}}}} \quad (1.3)$$

The goal of this thesis project was to investigate whether embedding Rydberg atoms into the plasma could be used to increase the Coulomb coupling parameter for the electrons

by countering the three body recombination. We investigated on the UNP evolved from cold nd_j ^{85}Rb Rydberg atoms ($24 \leq n \leq 120$). The Rydberg atoms were created from cold atoms in a magneto-optical trap which had a maximum density of $1 \times 10^{10} \text{ cm}^{-3}$ and temperature at around $100\mu\text{K}$. We ionized the Rubidium atoms using a Littman pulsed dye laser system and excited others to Rydberg states using a narrow-bandwidth pulsed laser. We were especially interested in using the plasma expansion velocity as a diagnostic to the UNP. In our experimental setup, we used a micro channel plate detector for detection of Rubidium ions in the plasma and we then derived the expansion velocity of the plasma given the ion time of flight spectroscopy.

Our first experimental interest is how accurately we can measure the expansion velocity based on the setup we have. We are also interested in whether it is possible to obtain an experimental value of Γ_e at $1 \mu\text{s}$ of plasma evolution time by measuring plasma expansion velocity at late times in plasma evolution. Thus, it became the method we initially used to find the expansion velocity using the ion time of flight signal. However, it can only measure the plasma's asymptotic expansion velocity (i.e. at a time $t > 50 \mu\text{s}$ in the plasma evolution process). Achieving information of the plasma immediately after its creation from that of the plasma in the later phase can help us understand the nature of the UNP as well. We were also interested in measuring the critical plasma parameter at any time after the plasma creation. Specially, we would like to see how the plasma expansion velocity changes during the plasma evolution [3].

1.3 Rydberg Atoms

As discussed in the previous section, Rydberg atoms may be often used in reversing the three body recombination which is a heating effect for the UNP. A Rydberg atom is an excited atom with one electron that has a very high principal quantum number. A Rydberg atom has an extremely large radius because the orbital radius r is proportional to n^2 . The long distance from the outer electron to the nucleus allows physicists to treat the Rydberg atoms as a Hydrogen-like atom. According to Bohr's correspondence principle, the behavior of the outer electron in a Rydberg atom is like that in classical mechanics, resulting in a long radioactive lifetime. An Rydberg atom will also be more sensitive to the electromagnetic field since the outer electron is away from the nucleus. In our context of the ultracold neutral plasma, Rydberg atoms are created by the three body recombination or by using a

narrow bandwidth laser.

Collisions between Rydberg atoms and electrons can either heat or cool the plasma. Specifically, if a collision excites a Rydberg atom to a higher n or ionizes it, the plasma will cool. On the other hand, if the atom is de-excited to a lower n , the plasma will be heater. The critical binding energy of Rydberg atoms for switching between cooling and heating is at $E_b = 2.7 \times k_B T_e$. [3]

1.4 Numerical Simulation

In addition to the experiments on the UNP, another significant part of this project was to carry out numerical simulations on the interaction of ions, electrons and Rydberg atoms in plasmas. Robicheaux introduced a numerical simulation model with a Monte Carlo model of Coulomb collisions, three-body recombination, and electron-Rydberg scattering. More information about the model can be found in Reference [16].

Based on Robicheaux's paper [16] and his simulation program, we are also able to perform simulations ourselves. Before we conduct any experiments, it is always beneficial to look at the numerical simulations. Thus, we used Robicheaux's program to see whether there is any relationship between the Γ_e value and expansion velocity 1 μs after the plasma formation and the Γ_e value and expansion velocity long after the plasma formation.

We are also interested in achieving plasma of relatively high Γ_e value ≈ 0.5 . Numerical simulation can help us understand how to achieve this experimentally. With a computer, we do not have to re-tune our laser all the times and we can get all the properties of the plasma from the output file of the simulation program. In particular, we would like to reproduce the results of Pohl's group [14]. Pohl used a computer program to simulate the UNP using 5×10^4 ions and 5×10^6 Rydberg atoms of $n = 100$. With the initial electron temperature $T_{e,0} = 6$ K, Pohl reported a peak in Γ_e value to more than 0.5 by adding another bunch of Rydberg atoms several μs after the initial creation of the plasma.

The results of their work can be found in Figure 1.3. We performed similar numerical simulation aiming for higher values of Γ .

In this honors project, we focused on two questions: Can we reach $\Gamma_e = 0.5$ at time 1 μs

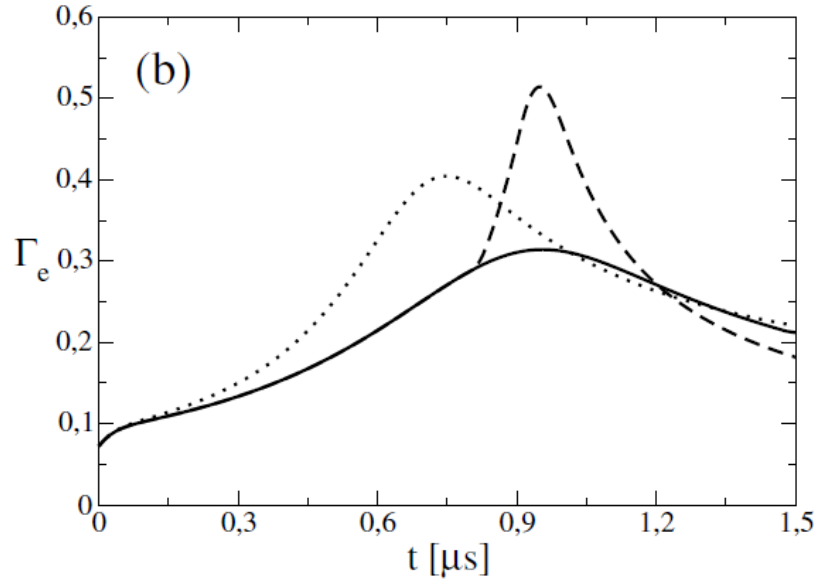


Figure 1.3: Results by Pohl's group, where the solid line is add 5×10^6 Rydberg atoms at $t = 0$; dotted line is adding some at $t = 0$ and some again the same number of Rydberg atoms using a $2 \mu s$ pulse; dashed line is adding some at $t = 0$ and some again the same number of Rydberg atoms at $t = 0.8 \mu s$ using a 100 ns pulse. [14]

plasma evolution time, and can we detect what we have done using our apparatus? We used both experiments and simulations to answer those two questions.

2. Experiment

2.1 Apparatus

In this section, I will talk about the apparatus in this honors thesis setup, the picture of which is shown in 2.1. There are three major parts of the lab: the magneto-optical trap, the laser cooling setup and the pulsed laser setup.

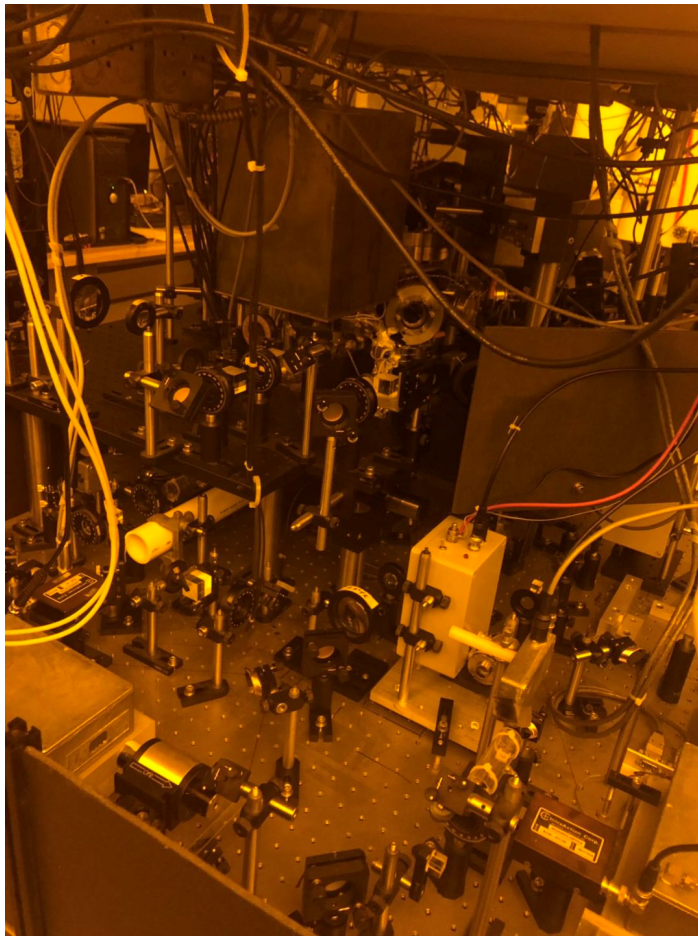


Figure 2.1: A photograph of the apparatus setup in our lab. The front are the cooling lasers and the back is the magneto-optical trap. The pulsed lasers are at the other side of the table.

2.1.1 Magneto-Optical Trap

As in most ultracold atom labs, we used a magneto-optical trap to cool and trap cold atoms. The MOT we used in our lab can trap Rubidium atoms up to a density of $5.0 \times 10^{10} \text{ cm}^{-3}$ with a temperature of $100 \text{ } \mu\text{K}$. [15]

The main setup of the MOT is the vacuum chamber in which the ultracold neutral plasma is made. The chamber can be evacuated to a pressure as low as 10^{-10} Torr or $1.3 \times 10^{-9} \text{ mbar}$ using an ion pump. The vacuum chamber has six windows through which the laser beams can be shone in all six directions as mentioned in the Introduction. The chamber is surrounded with anti-Helmholtz coils which are used to provide a spatially varying magnetic field inside the chamber. There is a Rubidium atom source providing Rb-85 for our experiment.

2.1.2 Laser Cooling

Narrow bandwidth lasers are required in laser cooling the Rubidium atoms for the accuracy of wavelength. In our lab, we used external cavity diode lasers and laser frequency stabilizing electronics to reach the required frequency stability. A normal diode laser would have a bandwidth high as $\Delta\nu/\nu \approx 2 \times 10^{-8}$, which was not acceptable because of the precise wavelength we needed for laser cooling. So, we used an external cavity to tune the laser to the wavelength we wanted and also to stabilize the frequency. We used a diffraction grating so that the first-order diffracted beam provides optical feedback to the laser's diode chip. We can determine the wavelength of the emission beam by rotating the diffraction grating.[13] We also used an injection locked laser diode to amplify the signal by the cooling laser.

We tuned the diode laser to a frequency $10 - 20 \text{ MHz}$ lower than the Rubidium-85 absorption frequency, which is the transition from $5s_{1/2}, F = 3$ state to $5p_{3/2}, F' = 4$, resulting in a wavelength of 780 nm . Because of the relativistic Doppler effect, only the atoms moving towards the laser would be blue-shifted to the diode laser frequency and absorb the photons. Because the emission of the photon would be in random direction and absorption of the photon would be in the opposite direction of the atom's motion, on average, the velocity of the atoms in that direction would decrease. We applied the cooling laser to all six directions $(+x, -x, +y, -y, +z, -z)$ of the vacuum chamber and so the magnitude of the velocity of the atoms was going to decrease, resulting in the atoms being colder.

With the diode lasers set up to that specific frequency, we were able to create cold

atoms; however, in order to take longer experiments, we need to stabilize the laser to the absorption frequency. A small proportion of the laser output was parsed through by a vapor Rubidium cell. The Rubidium cell absorbed the photons and reach to $5p_{3/2}, F' = 4$ state and then went back to the $5s_{1/2}, F = 3$ under spontaneous emission, emitting photons of the frequency we wanted. We observed the Doppler-free signals from both the cooling laser and the re-pump laser from the oscilloscopes and had laser-locking boxes to lock the laser at the emission frequency using a feedback loop to a piezoelectric element that precisely controlled the diffraction grating in the external cavity diode laser.

The optical alignment of the lasers can be seen in 2.2.

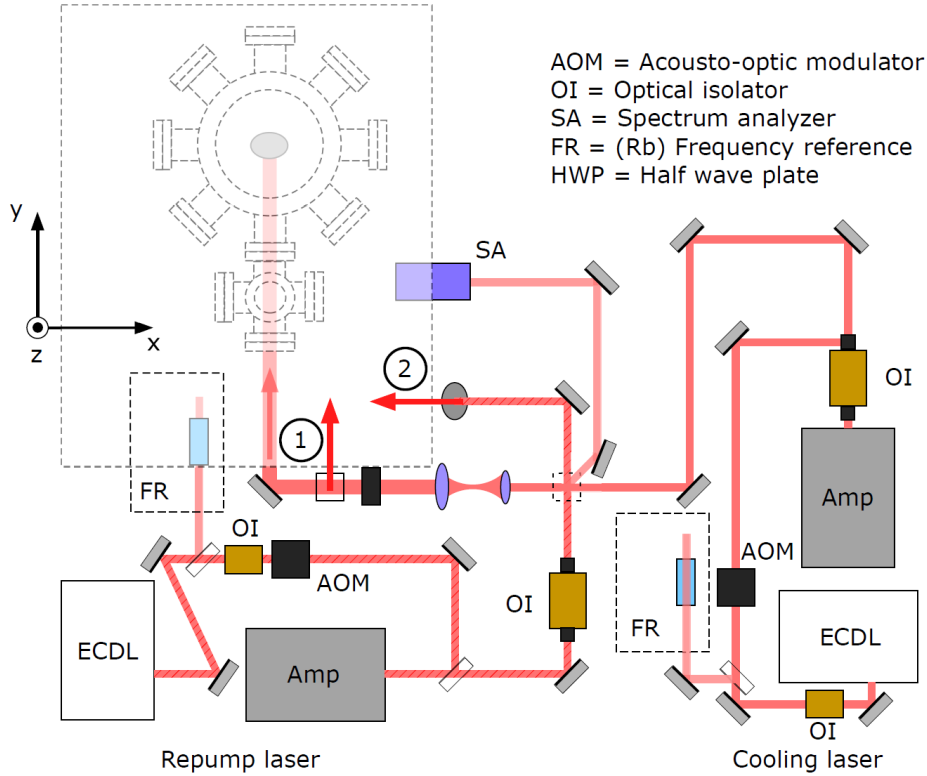


Figure 2.2: A schematic of the cooling laser setup in our lab made by professor Duncan A. Tate.

2.1.3 Photo Ionization and Excitation to Rydberg States

After successfully trapped the Rubidium ions, we needed to separate the ions and electrons as those are in a plasma and excite some of the electrons to Rydberg states (states of high principal quantum number $n \approx 40$), the schematic of which can be found in Figure 2.3. We

achieved creating the UNP by photo-ionization beyond the ionization limit using a Littman dye laser. The details of the Littman laser (i.e. pulsed tunable dye laser) can be found in Reference [9]. At a specific delay, We use a narrow-band pulsed laser to excite some of the Rubidium atoms in the $5p_{3/2}$ state to Rydberg states.

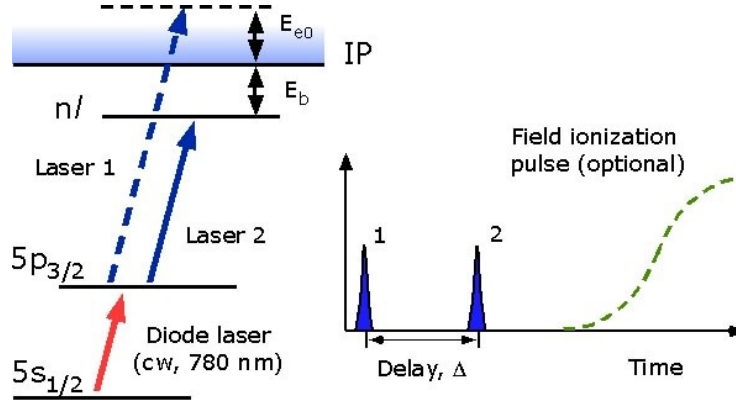


Figure 2.3: A schematic of the pulse laser setup in our lab, where laser 1 is the Littman laser used to perform photo-ionization and laser 2 is the narrow-band pulse laser to excite electrons to Rydberg states. Made by Professor Duncan A. Tate.

2.1.4 Detection of UNP

After the excitation of Rubidium atoms to Rydberg states, the plasma started to expand and we would like to observe the properties of the plasma by observing ions or electrons from the UNP. We used a field mesh and a micro-channel plate detector (MCP) to obtain the ion time of flight signal, the schematic of which is shown in Figure 2.4. The MCP was used to detect ions arriving at the detector. The MCP signal was proportional to dN_{out}/dt , where N_{out} is defined by Equation 1.2 [4]. As the plasma expands, we could field select ions by applying a negative voltage to the MCP mesh to attract all the ions to the direction of the MCP once they get out off the field meshes.

There are three places where we could apply voltages, the MCP mesh and the front and back of the field meshes, which allowed us to perform different kinds of measurements and tests. We could also delay the voltage apply time with respect to the laser pulse time using some timing electronics.

We also compensated for the electric field within the field meshes (we need to do that because if there was electric field within the meshes, the center of mass of the plasma would move either towards or away from the MCP, resulting in a earlier or later arrival time of the

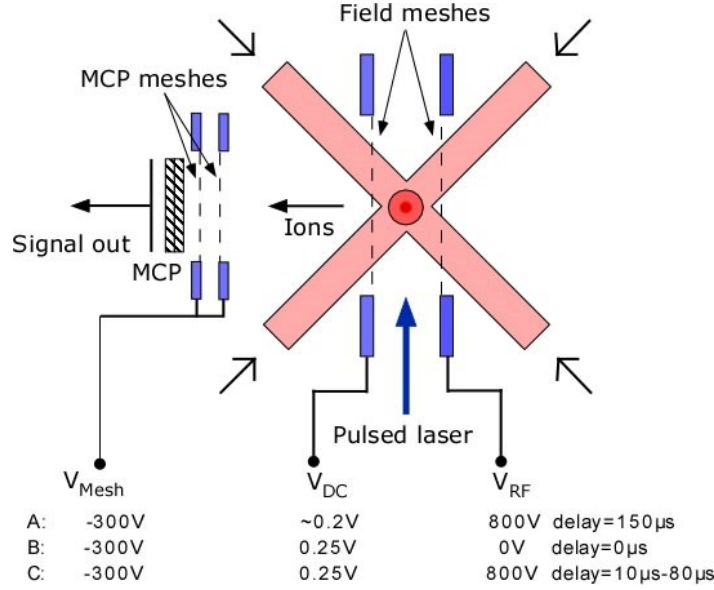


Figure 2.4: A schematic of the field meshes and MCP used for obtaining the ion time of flight signal. Details of different voltages setup are explained in text. Made by Duncan A. Tate.

electrons.) We are able to precisely determine what the compensate voltage we should put on the front of the field meshes. We used voltage setup A for calibration of the compensate electric field: $V_{\text{Mesh}} = -300\text{ V}$ on the MCP mesh, $V_{\text{RF}} = 800\text{ V}$ on the back of the field mesh and adjustable voltage V_{DC} on the front of the field mesh. We delayed the V_{RF} pulse by $\tau \approx 150\text{ }\mu\text{s}$ so that the plasma was able to expand before being all pushed to the micro-channel plate detector. If we have got the correct compensation voltage on V_{DC} , we should have maximized the signal of the MCP. A schematic comparison of different MCP signal from different compensation voltages can be seen in Figure 2.5, where we concluded that the correct compensation voltage for V_{DC} is 0.25 V.

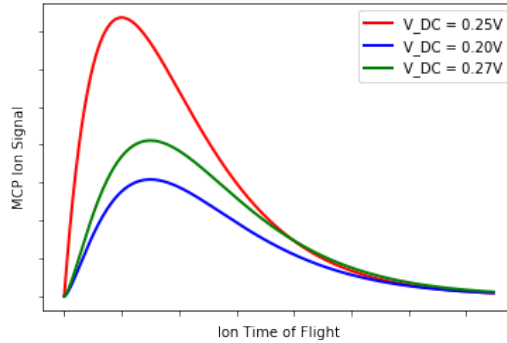


Figure 2.5: Schematics of adjusting the compensation voltage.

We could either use setup B or setup C for detection of the plasma property. For setup B, we set $V_{mesh} = -300$ V and $V_{DC} = 0.25$ V but we left the back of the field meshes grounded. In this case, we let the plasma expand freely within the field mesh and pushed the ions to the MCP once they reached outside of the field mesh after ≈ 30 μ s. We were going to get the ions distribution regarding the plasma $\approx 30 - 100$ μ s after its creation. For setup C, we set $V_{mesh} = -300$ V and $V_{DC} = 0.25$ V but we set $V_{RF} = 800$ V as we did in the calibration. Instead of delaying V_{RF} for 150 μ s, we delayed V_{RF} for $\tau = 0.4$ μ s – 100.4 μ s. In this case, we pushed all the ions to the MCP at a specific time after the plasma creation. From the MCP output, we could gather information of the plasma at a specific time even immediately after the plasma creation. We collected data using both of the setup and the results will be discussed in Chapter 4

2.1.5 Laser and Detection Synchronization

The experiments are synchronized using RS DG-535 and DG-645 digital delay generators. The synchronization equipment includes the DG-645 Digital Delay Generators triggered by one of the DG-535 timers. The delay generators synchronize, with sub nanosecond precision, the firing of the narrow bandwidth laser, the firing of the Littman laser, switching off the anti-Helmholtz coils, and the voltage delay for detection purpose. The experiments are repeated every 50 ms.

2.2 Procedure of Operation

To create a UNP with the specific properties, (e.g. initial electron temperature and ionization fraction), we needed to follow a procedure to setup the apparatus. First, we needed to warm up the pulse laser used in the experiment. The flashlight of both of the pulse lasers needed about 20 minutes to warm up. Second, we needed to release Rubidium atoms to the MOT and recall the setup for time delay equipment. After that, we should lock the laser by the laser locking boxes. The laser locking boxes took in the electric signal by the Rb Frequency reference in Figure 1.2 and locked the laser to 10 – 20 MHz below the absorption line of the Rubidium cell. At this point, we should see a cold atom cloud on the monitor like that in Figure 2.6 and we could then begin to create the UNP using the pulsed laser.

To detect properties of the UNP, we needed to recover the voltage setup for the MCP-field mesh system. Then we used the computer to record the oscilloscope output for the signal

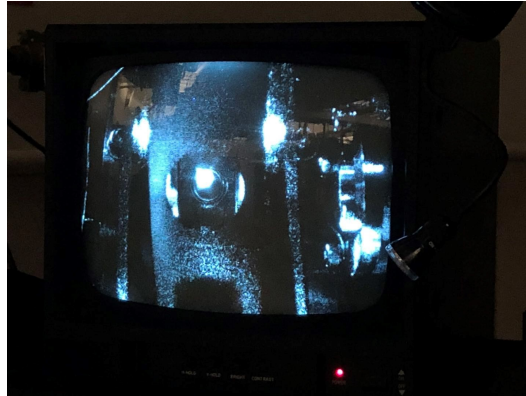


Figure 2.6: Photograph of 780 nm fluorescence from cold Rydberg atoms.

from the MCP. At this point, we finished the experiment and the collection of the data and we were ready to proceed to data analysis.

3. Numerical Simulation

As I mentioned before in the Introduction section, numerical simulation sometimes can provide information of the UNP that cannot be collected experimentally with our Rubidium atoms. To further understand the UNP, we used the computer program written by Professor Francis Robicheaux of Purdue University in C++ to simulate the UNP expansion.[16, 17]

3.1 Hanson/Robicheaux program

The UNP simulation program by Professor Robicheaux incorporates three-body recombination, electron-Rydberg scattering and angular momentum changing collisions to simulate the electron distribution some time after the plasma creation. The code snippet is included below in Figure 3.1. The output file include the property of the plasma at each time and a sample of the output is included in Figure 3.2. The 0-th column is the time step when the data is recorded; the 1-st column is the average atom spacing within the plasma which characterize the number density of the UNP; the 2-nd column is the debye length; the 3-rd column is the Coulomb coupling parameter, Γ ; the 4-th column is the electron temperature; the 5-th column is the number of Rydberg atoms; the 6-th column is the change in the number of atoms with $n \leq 5$ since previous report; the 7-th column and the 8-th column are the same with $\beta = \eta = \frac{1}{2\sigma^2}$. From the output file, we are able to determine the expansion velocity of the plasma $v = \frac{1}{\sqrt{2}} \frac{n^{-1/2}}{t} \cdot \frac{\Delta n^{-1/2}}{\Delta t}$, and so $T_{e,0} = \frac{m_e v^2}{k_B} = 0.005143 \cdot \frac{n^{-1/2}}{t} \cdot \frac{\Delta n^{-1/2}}{\Delta t}$ describes the effective electron temperature of the plasma.

```

//the following block is for adding the Rydberg atom
if ((iadd == 0) && ((itim*dtim) > tadd))
{
    iadd = 1;
    for (j = 0; j <= numrydadd; j++)
    {
        rydprm[0][numryd] = erydn;
        rydprm[1][numryd] = scale*sqrt(SimRan1(i1, i2));
        rydprm[2][numryd] = 0.0;
        dum1 = 2.0*pi*SimRan1(i1, i2);
        dum2 = sqrt(-log(SimRan1(i1, i2)) / eta0);
        rydprm[3][numryd] = dum2*cos(dum1);
        rydprm[4][numryd] = 0.0;
        rydprm[5][numryd] = 0.0;
        latom[numryd] = 2; // Angular momentum of added Rydbergs
        numryd++;
    }

    xnum += numrydadd*rydfrac; numrecomtot += numrydadd*rydfrac;
}
//end of block for adding Rydberg atoms

```

(a) Adding Rydberg atoms

```

// TBR step from Muller and Wolf Eqs 31-33
// compute the number of TBR during time step
// nstar is the n_cut off, nstar7 is nstar^7
nstar = sqrt(13.6*echrg / (2 * temp)); nstar7 = pow(nstar, 7);
// dum2 is the factor that comes from integrating the Gaussian density
// with the density dependence of the TBR rate
dum2 = (xnum - numrecomtot)*beta / (sqrt(3.0)*pi);
dum3 = (xnum - numrecomtot)* eta / (sqrt(3.0)*pi);

// numrecom is the number of recombined atoms during this time step
// plus any fractional electrons from previous steps
numrecom += nstar7*2.8e-42*dum2*dum2*dum3*dtim*(echrg / temp);

// convert to integer number of Rydberg "atoms"
dum2 = numrecom / rydfrac; jj = int(dum2); numrecom -= double(jj)*rydfrac;

// numrecomtot is the total number of recombined atoms
numrecomtot += double(jj)*rydfrac;

```

(b) Part of the three body recombination simulation

Figure 3.1: Code snippet for simulation program.

Time	a	λ_D	Γ	T_e	N_R	ΔN_s	$\beta^{1/2}$	$\eta^{1/2}$
0	1	2	3	4	5	6	7	8
2.00E-07	9.38E-06	3.92E-05	1.91E-02	9.35E+01	2.29E+04	6.98E+02	3.05E-04	3.05E-04
6.00E-07	9.78E-06	3.93E-05	2.07E-02	8.27E+01	2.06E+04	5.04E+02	3.20E-04	3.20E-04
1.00E-06	1.04E-05	4.01E-05	2.26E-02	7.08E+01	1.90E+04	3.60E+02	3.42E-04	3.42E-04
1.40E-06	1.13E-05	4.14E-05	2.48E-02	5.96E+01	1.79E+04	3.34E+02	3.71E-04	3.71E-04
1.80E-06	1.23E-05	4.32E-05	2.72E-02	4.99E+01	1.73E+04	2.22E+02	4.05E-04	4.05E-04
2.20E-06	1.35E-05	4.51E-05	2.97E-02	4.18E+01	1.69E+04	1.92E+02	4.43E-04	4.43E-04
2.60E-06	1.47E-05	4.73E-05	3.22E-02	3.53E+01	1.66E+04	2.02E+02	4.84E-04	4.84E-04
3.00E-06	1.60E-05	4.96E-05	3.47E-02	3.01E+01	1.64E+04	1.46E+02	5.27E-04	5.27E-04
3.40E-06	1.74E-05	5.19E-05	3.73E-02	2.58E+01	1.62E+04	1.54E+02	5.72E-04	5.72E-04
3.80E-06	1.88E-05	5.42E-05	4.00E-02	2.22E+01	1.60E+04	1.36E+02	6.18E-04	6.18E-04
4.20E-06	2.02E-05	5.65E-05	4.27E-02	1.94E+01	1.59E+04	1.34E+02	6.66E-04	6.66E-04
4.60E-06	2.17E-05	5.88E-05	4.53E-02	1.70E+01	1.57E+04	1.28E+02	7.14E-04	7.14E-04
5.00E-06	2.32E-05	6.11E-05	4.80E-02	1.50E+01	1.56E+04	1.08E+02	7.63E-04	7.63E-04
5.40E-06	2.47E-05	6.33E-05	5.06E-02	1.34E+01	1.55E+04	1.10E+02	8.13E-04	8.13E-04

Figure 3.2: Sample output of the simulation program.

3.2 Simulation Process

We did two sets of numerical simulations during this project: Specifically, we added Rydberg atoms at two different times to see the effect on the plasma properties. We also investigated the correlation between the Coulomb coupling parameter earlier in the plasma evolution with the subsequent plasma expansion velocity.

3.2.1 Adding Rydberg Atoms twice

The first thing we tried was adding Rydberg atoms twice, trying to replicate the results by the Pohl's group [14]. We set the principal quantum number of the Rydberg atoms to $n = 40$ and the proportion of Rydberg atoms to ions to 100, which means that there would be 100 times more Rydberg atoms than ions. There are 3×10^5 ions and the initial electron temperature is set to 100 K. We added the first bunch of Rydberg atoms at time $t = 0$ and we added the second bunch of them at time $t = 0 \mu s, 0.2 \mu s, 0.8 \mu s, 2 \mu s$. Here, we were trying to see whether there would be a significant increase in the Coulomb coupling parameter Γ as it did in the Pohl's group in Figure 1.3.

3.2.2 Delaying the Addition of Rydberg atoms

As we mentioned before, we were interested in whether there would be any relationship between the Γ_e value $1 \mu s$ after the plasma formation and the Γ_e value long after the plasma formation (i.e. whether we could predict the early stage of plasma evolution using the data

we got at a later stage of plasma evolution, as we did using the voltage setup B in the experiments we have done.)

To achieve a more significant results, we set the principal quantum number of the Rydberg atoms to $n = 28$ and the proportion of Rydberg atoms to ions to 1. We have 3×10^8 ions and the initial electron temperature is 100 K. This time, we added the Rydberg atoms at $t = 0, 0.5 \mu s, 1 \mu s, 2 \mu s, 3 \mu s, 4 \mu s, 5 \mu s, 10 \mu s, 80 \mu s$. We were trying to compare the effective electron temperature $T_{e,0}$ and the Coulomb coupling parameter at $t \approx 30 \mu s$ to see whether we could recover the time delay setup we used.

The results of all simulations are included in Chapter 4.

4. Results

In this chapter, I will be talking about results we obtained from the experiments and numerical simulations described in Chapter 3.

We have 2 sets of simulation data:

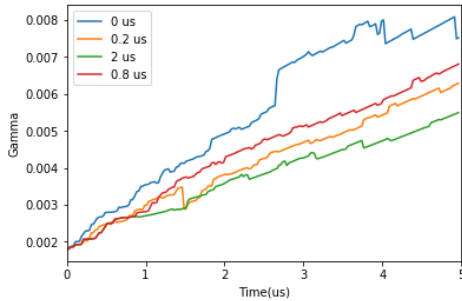
1. Adding Rydberg atoms twice to achieve high $\Gamma_e > 0.5$.
2. Does Γ_e at $1 \mu s$ correlate with v_0 at later times?

We also have two sets of experimental data:

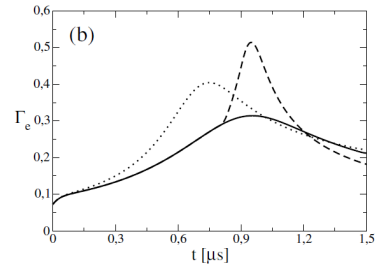
1. Measuring the expansion velocity using setup B in Figure 2.4.
2. Measuring the expansion velocity using setup C in Figure 2.4.

4.1 Simulation Data - 1

In Chapter 1 and Chapter 3, we talked about reproducing the results by the Pohl's group about adding Rydberg atoms twice to have a boost in the Coulomb coupling parameter. Our results are shown in Figure 4.1 with all four experiments add Rydberg atoms at time $t = 0$ and different colors of lines suggest adding another bunch of Rydberg atoms at time $t = 0, 0.2 \mu s, 0.8 \mu s, 2 \mu s$ after the plasma creation.



(a) Our Simulation results



(b) Pohl's group's simulation results

Figure 4.1: Simulation results trying to achieve a high Coulomb coupling parameter. Details of the Pohls group results can be found in Figure 1.3.

From those figures, we figured out that we did not achieve the same boost as the Pohl's group did. The reason behind it was that the program designed by Prof. Robicheaux has a

certain limitation for the total number of ions and electrons it could handle ($\approx 1 \times 10^9$), and so we can only achieve a Coulomb coupling parameter < 0.01 with the same setup as the Pohl's group (i.e. $\frac{N_{Ryd}}{N_{ion}} = 100$). The limitation of the program prevented us from reproducing the same results as in Pohl's group.

4.2 Experimental Data - 1

In Chapter 2, we discussed two ways of measuring the plasma using voltage setup B and setup C in Figure 2.4 after the creation of the UNP. Setup B allows us to get the ions distribution regarding the plasma $\approx 30 - 100 \mu s$ after its creation. Setup C allows us to gather information of the plasma at a specific time even immediately after the plasma creation.

First, we will talk about data collected by setup B, which is shown below in Figure 4.2. The full data are presented in blue while the data used in fitting are presented in green. The red line is the fitted line of the oscilloscope signal using

$$\text{Signal} = \frac{d(N_{out})}{dt}, N_{out} = \int_d^\infty \int_{-\theta_0}^{\theta_0} n_i(r, t) d\theta dr, n_i(r, t) = \frac{N_i}{(2\pi\sigma^2)^{3/2}} e^{-r^2/2\sigma^2} \quad (4.1)$$

where $\sigma = \sqrt{\sigma_0^2 + v^2 t^2}$ as we talked about in Chapter 1. Here, we are trying to fit the data so that we can reduce the expansion velocity v of the plasma. From the fitting results in Figure 4.2, we can figure out that for a high ionization laser power [Using data002, more information needed], we have the expansion velocity $v = 90.91 \text{ m/s}$ while for a low ionization laser power [Using data006], we have the expansion velocity $v = 68.52 \text{ m/s}$.

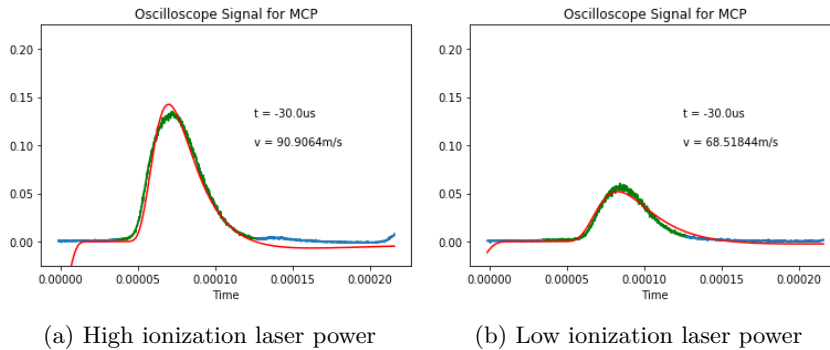


Figure 4.2: Oscilloscope output for different ionization laser power.

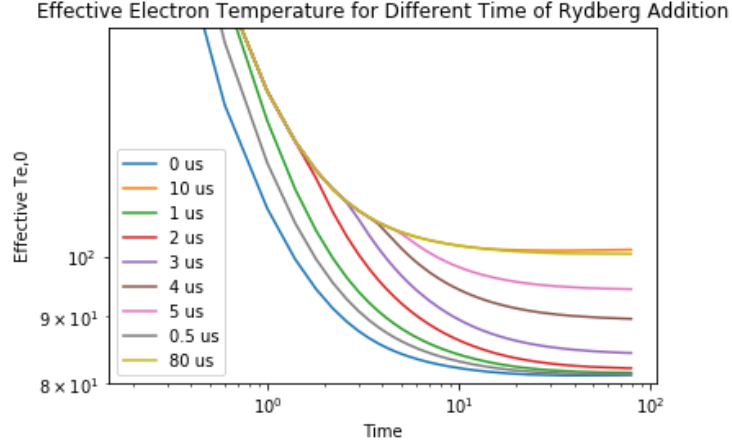
We noticed that the fitting is not so great: the data points seem to be more centered than the fitted points and we do not have the same expansion velocity deduced from the high laser power and the low laser power. The difference between the expansion velocities is out of our expectation: we expected the expansion velocities to be the same since we only vary the ionization power of the plasma, which should yield the same expansion velocity. We suspected the reason being behind the fitting mechanism we are using. We assumed that the electric field between the MCP meshes and the meshes is uniform so that the ions that could get into the MCP are exactly those in the cone within the integral limits. However, in the MOT setup, the voltage source we were using was not guaranteed to generate a uniform electric field. As a result, the fitting we have done may not be accurate enough to reflect the characteristics of the plasma.

4.3 Simulation Data - 2

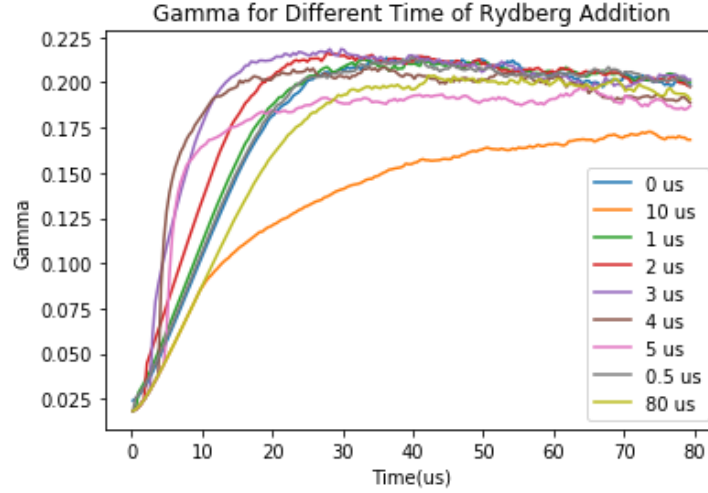
Since setup B could only provide us with property of the plasma $\approx 30\mu s$ after its creation, we were concerned that whether we were able to trace the property of the plasma immediately after the plasma creation from the data we collected in a later stage of the plasma evolution. As a result, we looked at the simulation data we collected in Chapter 3.2.2.

In order to test whether the prediction works, we plotted the effective electron temperature $T_{e,0}$ versus time and the Coulomb coupling parameter Γ_e versus time as in Figure 4.3. Different colored lines mean different item when adding Rydberg atoms with a delay from $0\mu s$ to $10\mu s$ with the yellow line not adding Rydberg atoms at all.

From Figure 4.3, subfigure (a), we can see that at time $t = 80 \mu s$, the effective electron temperatures for different Rydberg addition scenarios are so different that we can correlate them back to the plasma conditions around time $t = 1 \mu s$. However, by looking at subfigure (b), we can see that although the Coulomb coupling parameters behave significantly different from time $t = 0$ to $t = 20 \mu s$, they all converge to $\Gamma_e \approx 0.2$ and start from the same value of $0.025 < \Gamma_e < 0.05$. The only significant effect that can be seen is that the added Rydberg atoms affect the rate at which the plasma reaches $\Gamma_e \approx 0.2$ value that is primarily due to the adiabatic expansion.



(a) Effective Electron Temperature



(b) Coulomb Coupling Parameter

Figure 4.3: Plasma with different initial conditions examined at later stage of evolution.

4.4 Experimental Data - 2

From the previous section 4.3, we know that we cannot trace back to the early stage of the plasma evolution from data we collected from the plasma at a late stage of evolution. So, the experimental methods we used in section 4.2 about tracking the plasma expansion starting at time $t > 30 \mu s$ may not provide us as valuable information about the early stage of the plasma. The solution to the problem comes from setup C of the voltages on the meshes. where we delay V_{RF} for $\tau = 0.4 \mu s - 100.4 \mu s$ to push all the ions to the MCP at a specific time after the plasma creation. In this case, we are able to get information about the plasma at a specific time even immediately after the plasma creation. The results we have got are shown in Figure 4.4.

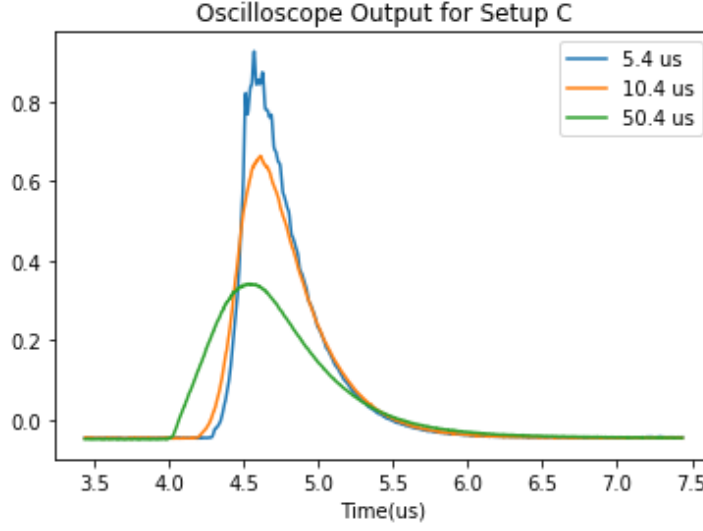


Figure 4.4: Oscilloscope output for different time delay in setup C.

From Figure 4.4, we can see that the data were more spread out for longer delay and the fronts of the signal were drastically different for different time delay. Those can be explained by that after a certain time of plasma expansion, the ions that are going towards the MCP can be accelerated for a shorter amount of time than those going towards the back of the field meshes. As a result, ions in the later stage of plasma expansion will have a larger variety of velocity, resulting a larger range of time when they arrive at the MCP. As the delay time of V_{RF} gets larger and larger, there will be more atoms closer to the back of the field mesh (longer acceleration time when applied the electric field), resulting in more atoms coming at a earlier time to the MCP.

5. Discussion

Now, we are able to answer the two questions we discussed at the end of Chapter 1.

5.1 Can we reach $\Gamma_e = 0.5$ at time $1 \mu s$ plasma evolution time by simulation?

The question was inspired by looking at Pohl's group's data in Figure 1.3 where he calculated the time evolution of a plasma of size $600 \mu m$ with 5×10^4 ions and 5×10^6 Rydberg atoms. The initial electron temperature was set to 6 K. He found a spike in the Coulomb coupling parameter if he added another group of Rydberg atoms using a 100 ns pulse at time $t = 0.8 \mu s$, higher than if adding at time $t = 0$.

We performed similar simulation using program provided by Professor Robicheaux of Purdue University. Unfortunately, we found our results were limited by the electrons and ions density in the program. The density was not large enough so that the electrons can interact more with Rydberg atoms to achieve a high Γ_e value.

In our experimental setup, we would be able to perform something similar but we would need to modify the approach. First, instead of creating a plasma by photionization and then adding Rydberg atoms at $t=0$, we would need to make UNP from cold Rydberg sample which evolves to plasma. Second, we can add Rydberg atoms at $t = 800$ ns in a 10 ns burst, but not over 100 ns in our pulsed laser system.

5.2 Can we infer Γ_e at $1 \mu s$ from the plasma expansion velocity by both simulation and experiment?

First, since we cannot get the expansion velocity or the effective electron temperature directly from the plasma as we did in a simulation, we would like to investigate on how reliable the experimental techniques are for finding the ion expansion velocity from the ion time of flight signals. At the start of this project, we tried to see a very slowly expanding UNPs from cold Rydberg samples using the pulsed laser setup. However, there seemed to be a minimum expansion velocity we could see, which is significantly higher than the one

we need to be sensitive to. We then were aware that our old method of getting expansion velocity from the ions TOF signal might not be as reliable as it needed to be.

As a result, we would like to re-calibrate the ions TOF signal by making UNPs through direct photoionization (i.e. without excitation to Rydberg atoms) using the Littman laser. We tried different fitting routines for the ion time of flight data other than Equation 4.1 including a cylindrical integral area than a spherical one. We also thought about how the electric field lines are distributed between the MCP meshes and the field meshes and how they could affect our area of integral. Unfortunately, the results for the plasma expansion velocity we got from the fitting are very sensitive to the different bias voltages we use (Figure 4.2), principally those on the MCP meshes, and the other fitting routines did not work either theoretically or experimentally. There might also be a focusing/de-focusing effect due to the MOT's magnetic field.

Second, since what we were measuring was plasma properties at a late stage of plasma evolution ($t > 30 \mu\text{s}$), we would like to see whether this is correlated with what we were interested in (i.e. the Coulomb coupling parameter at $1 \mu\text{s}$). Consequently, we ran a simulation to see whether we could get a correlation between the Γ_e value at early time with the expansion velocity (or the effective electron temperature) at late time. It turns out that we cannot make such prediction as the correlation between the two is not strong in Figure 4.3.

Knowing that we would not be able to get Γ_e from the expansion velocity at late stage of plasma evolution, we switched to see whether we could get the expansion velocity using setup C and we got results as in Figure 4.4. The results look promising as discussed in Chapter 4 but more work needs to be done. It seemed like that the measured expansion velocities depend on the size of the pulsed voltage, which may be due to Coulomb defocusing. The arrival times of the ions at the MCP is reversed from their initial spatial distributions (i.e. ions initially nearer MCP arrive later). Hence, rear of ion cloud passes through front, increasing Coulomb repulsion after the plasma is quenched by electric field pulse which might lead to inaccurate expansion velocities being measured.

6. Conclusion and Future Work

Aiming for achieving a larger Coulomb coupling parameter to study the strong-coupled ultracold neutral plasma, we tried different things either experimentally or numerically. First, we tried to replicate the results by the Pohl's group [14] of achieving high Coulomb coupling parameter by adding Rydberg atoms at different time. After realizing that our computational power limits us to achieve a high Γ_e by simulation, we turned to experiments to test whether we could gather precise information about the plasma expansion (i.e. the expansion velocity). We discovered a nice way of figuring out how to compensate outside electric field for better measurement of the expansion velocity. With the help of the simulation program, we also discovered that we cannot trace back the plasma behavior by information of the plasma that we collected at a later time of the plasma evolution. In order to get the plasma information even immediately after the plasma creation, we discovered a new method by pushing all the ions in the plasma with a voltage pulse of a time delay.

For the future, we are ready to explore our new method of measuring the expansion velocity by trying to come up with a model and trying to address the problems we talked about by the end of Chapter 5. After we get the precise measurement of the expansion velocity, we can design more experiments trying to achieve a more strongly-coupled UNP. We would also like to improve the numerical simulation by trying to modify the program to achieve a higher electrons and ions density for higher Coulomb coupling parameter for electrons.

A. Computer Science Capstone Experience

This project cannot be completed without the help of computing and computation. In this chapter, I will talk about how this project is completed with the help of computer science knowledge.

First of all, the simulation program by Professor Robicheaux is written in C++ and the CS course "Programming Languages" helped me a lot in dealing with the simulation program. I also modified the program so that it served the purpose in this project. For example, I added a second time of adding Rydberg atoms similar to Figure 3.1. I also added more lines to the code to either let the program print more information about the simulation or write down it as a file. The figure of part of my modification to the code can be found in Figure A.1

```
// edited by Yin Li to print the number of Rydberg atoms for each timestep
printf("number of Rydbergs = %i \n", numryd);
}
} //for(itim = 1 ; itim <= numtim ; itim++)
// edited by Yin Li to record the energy distribution
for (j = 0; j < numryd; j++) {
    fprintf(outtest, "%13.6E \n", rydprm[0][j]);
}
//end of editing
```

Figure A.1: Modification I made of the simulation program.

Second, I used Jupiter Notebook for analyzing the data and producing figures as those in Chapter 4. I used pandas for file reading, numpy for data analyzing, and pyplot for data plotting. An example program is posted in Figure A.2, Figure A.3, and Figure A.4 to create Figure 4.3. I used code like Figure A.5 to fit the data by lmfit.

```

In [1]: import matplotlib.pyplot as plt      # use matplotlib for plotting function
import pandas as pd                        # use pandas for reading datafiles
import numpy as np
import sys                                # only needed to determine Python version number
import matplotlib                          # only needed to determine Matplotlib version number
import glob                                # file name pattern matching functionality
import math                                # math library; warning - may overlap with numpy!

# Enable inline plotting
%matplotlib inline

print('Python version ' + sys.version)
print('Pandas version ' + pd.__version__)
print('Matplotlib version ' + matplotlib.__version__)

Python version 3.7.1 (v3.7.1:260ec2c36a, Oct 20 2018, 14:05:16) [MSC v.1915 32 bit (Intel)]
Pandas version 0.23.4
Matplotlib version 3.0.1

In [2]: # file loading
Files_28 = []
filelist = glob.glob('28\\*.dat')
print(filelist)
for i in range(0, len(filelist)):
    Files_28.append(filelist[i])

Files_45 = []
filelist = glob.glob('45\\*.dat')
print(filelist)
for i in range(0, len(filelist)):
    Files_45.append(filelist[i])

Files_35 = []
filelist = glob.glob('35\\*.dat')
print(filelist)
for i in range(0, len(filelist)):
    Files_35.append(filelist[i])

['28\\plaspar0Rb80d_3.0E8_100_300_0_800.dat', '28\\plaspar0Rb80d_3.0E8_100_300_10_20.dat', '28\\plaspar0Rb80d_3.0E8_100_300_10_800.dat', '28\\plaspar0Rb80d_3.0E8_100_300_20_800.dat', '28\\plaspar0Rb80d_3.0E8_100_300_30_800.dat', '28\\plaspar0Rb80d_3.0E8_100_300_40_800.dat', '28\\plaspar0Rb80d_3.0E8_100_300_50_800.dat', '28\\plaspar0Rb80d_3.0E8_100_300_5_800.dat', '28\\plaspar0Rb80d_3.0E8_100_300_800_800.dat']
['45\\plaspar0Rb45d_3.0E8_100_300_0.dat', '45\\plaspar0Rb45d_3.0E8_100_300_10.dat', '45\\plaspar0Rb45d_3.0E8_100_300_10_20.dat', '45\\plaspar0Rb45d_3.0E8_100_300_20.dat', '45\\plaspar0Rb45d_3.0E8_100_300_25_50.dat', '45\\plaspar0Rb45d_3.0E8_100_300_80_0.dat']
['35\\plaspar0Rb35d_3.0E8_100_300_0.dat', '35\\plaspar0Rb35d_3.0E8_100_300_10.dat', '35\\plaspar0Rb35d_3.0E8_100_300_15.dat', '35\\plaspar0Rb35d_3.0E8_100_300_20.dat', '35\\plaspar0Rb35d_3.0E8_100_300_30.dat', '35\\plaspar0Rb35d_3.0E8_100_300_40.dat', '35\\plaspar0Rb35d_3.0E8_100_300_5.dat', '35\\plaspar0Rb35d_3.0E8_100_300_50.dat', '35\\plaspar0Rb35d_3.0E8_100_300_800.dat']

```

Figure A.2: Code to import packages and load files.

```

In [3]: # file reading
dfs_list_28 = []
for i in range(len(Files_28)):
    dfs_list_28.append(pd.read_csv(Files_28[i], sep='s+'))

dfs_list_45 = []
for i in range(len(Files_45)):
    dfs_list_45.append(pd.read_csv(Files_45[i], sep='s+'))

dfs_list_35 = []
for i in range(len(Files_35)):
    dfs_list_35.append(pd.read_csv(Files_35[i], sep='s+'))

In [4]: # calculate Te,0
# Te,0 = (0.010286/2)*(n^0.5/t)*(dn^0.5/dt)
T_list_28=[]
for j in range(len(dfs_list_28)):
    dfs=dfs_list_28[j]
    lst=[]
    for i in range(len(dfs['0'])-1):
        lst.append((0.010286/2)*(dfs['7'][i]/dfs['0'][i])*(dfs['7'][i+1]-dfs['7'][i])/(dfs['0'][i+1]-dfs['0'][i]))
    T_list_28.append(lst)

T_list_45=[]
for j in range(len(dfs_list_45)):
    dfs=dfs_list_45[j]
    lst=[]
    for i in range(len(dfs['0'])-1):
        lst.append((0.010286/2)*(dfs['7'][i]/dfs['0'][i])*(dfs['7'][i+1]-dfs['7'][i])/(dfs['0'][i+1]-dfs['0'][i]))
    T_list_45.append(lst)

T_list_35=[]
for j in range(len(dfs_list_35)):
    dfs=dfs_list_35[j]
    lst=[]
    for i in range(len(dfs['0'])-1):
        lst.append((0.010286/2)*(dfs['7'][i]/dfs['0'][i])*(dfs['7'][i+1]-dfs['7'][i])/(dfs['0'][i+1]-dfs['0'][i]))
    T_list_35.append(lst)

```

Figure A.3: Code to read files and calculate the effective electron temperature of the UNP.

```
In [5]: fig, ax = plt.subplots(1,3,figsize=(18,6))

for i in range(len(dfs_list_28)):
    ax[0].loglog(dfs_list_28[i]['0'][:199],T_list_28[i],label=Files_28[i][31:])

for i in range(len(dfs_list_35)):
    ax[1].loglog(dfs_list_35[i]['0'][:199],T_list_35[i],label=Files_35[i][31:])

for i in range(len(dfs_list_45)):
    ax[2].loglog(dfs_list_45[i]['0'][:199],T_list_45[i],label=Files_45[i][31:])

ax[0].set_ylim(60, 150)
ax[1].set_ylim(60, 150)
ax[2].set_ylim(60, 150)
ax[1].set_xlabel("Time (s)")
ax[0].set_ylabel("Te,0")
ax[0].legend()
ax[1].legend()
ax[2].legend()
```

```
Out[5]: <matplotlib.legend.Legend at 0xdba7ff0>
```

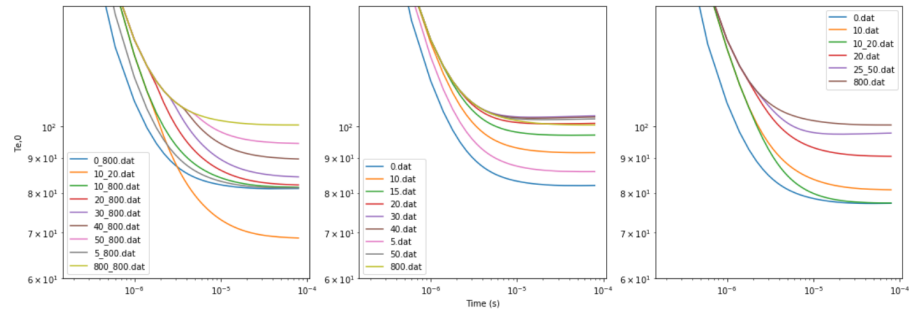


Figure A.4: Code to plot the data.

```
In [25]: def g(x, v0, vf, tao, Ni, a):
v = vf + (v0-vf)*np.exp(-(x+a)/tao)
sigma = np.sqrt(sigma_0**2+v**2*(x+a)**2)
N = (0.5 * Ni * (v**2*(x+a)) / sigma**4 *
      (np.sqrt(2/(np.pi))*sigma*d*(1-np.exp(-R**2/(2*sigma**2))))*
      np.exp(-d**2/(2*sigma**2)) + R**2*(scipy.special.erf(d/(np.sqrt(2)*sigma))-1)*
      np.exp(-R**2/(2*sigma**2))))
return N

offset = pd.read_csv("pl012716000.csv",header=None)
data = pd.read_csv("pl012716001.csv",header=None)
data[4] = data[4] - offset[4]
x = data[3][550:1300]
y = data[4][550:1300]
mod = Model(f)
params = mod.make_params(v = 100, Ni = 1e-5, a = 0)
params['v'] = Parameter(name='v', value=100)
ret = mod.fit(y, params, x=x)
print(ret.fit_report())

plt.plot(data[3][500:1600], data[4][500:1600], color = "black")
plt.plot(x,y, color = 'blue')
plt.plot(data[3][500:1600],f(data[3][500:1600], ret.best_values['v'], ret.best_values['Ni'], ret.best_values['a']), color = 'red')
#plt.plot(x,f(x, ret.best_values['v'], ret.best_values['Ni'], 0))

mod2 = Model(g)
params = mod2.make_params(v0 = 0, vf= 100, tao = 1e-5, Ni = 1, a = 0)
params['v0'] = Parameter(name='v0', value=1, min = 0.1, max = 100)
ret = mod2.fit(y, params, x=x)
print(ret.fit_report())
plt.plot(data[3][500:1600],g(data[3][500:1600], ret.best_values['v0'], ret.best_values['vf'], ret.best_values['tao'],ret.best_va
```

Figure A.5: Code to fit the data.

B. Physical Review A Paper

This appendix concerns the paper I co-authored before the start of the honors thesis which brought me to the field of ultracold neutral plasma and is relevant to this project. The paper was published in Physical Review A in 2018 [4]. I helped with data collection of the relation between the effective electron temperature and the mean Rydberg atom spacing for different Rydberg states. For the numerical simulation part, we used the same program from Professor Robicheaux of Purdue University and I helped ran the simulation program to simulate our experimental setup.

The honors thesis was based on the continuation of this paper. We asked the question that whether we could extend our scope of the Coulomb coupling parameter to 0.5 at time $1\ \mu s$ after the plasma creation. We were also interested in whether it would be possible to get a value of Γ_e at $1\ \mu s$ from the expansion velocity at later time in the plasma evolution.

PHYSICAL REVIEW A **97**, 043401 (2018)**Expansion of an ultracold Rydberg plasma**Gabriel T. Forest,¹ Yin Li,¹ Edwin D. Ward,¹ Anne L. Goodsell,² and Duncan A. Tate^{1,*}¹*Department of Physics and Astronomy, Colby College, Waterville, Maine 04901, USA*²*Department of Physics, Middlebury College, Middlebury, Vermont 05753, USA*

(Received 5 February 2017; revised manuscript received 6 March 2018; published 2 April 2018)

We report a systematic experimental and numerical study of the expansion of ultracold Rydberg plasmas. Specifically, we have measured the asymptotic expansion velocities, v_0 , of ultracold neutral plasmas (UNPs) which evolve from cold, dense samples of Rydberg rubidium atoms using ion time-of-flight spectroscopy. From this, we have obtained values for the effective initial plasma electron temperature, $T_{e,0} = m_{\text{ion}} v_0^2 / k_B$ (where m_{ion} is the Rb^+ ion mass), as a function of the original Rydberg atom density and binding energy, $E_{b,i}$. We have also simulated numerically the interaction of UNPs with a large reservoir of Rydberg atoms to obtain data to compare with our experimental results. We find that for Rydberg atom densities in the range 10^7 – 10^9 cm^{-3} , for states with principal quantum number $n > 40$, $T_{e,0}$ is insensitive to the initial ionization mechanism which seeds the plasma. In addition, the quantity $k_B T_{e,0}$ is strongly correlated with the fraction of atoms which ionize, and is in the range $0.6 \times |E_{b,i}| \lesssim k_B T_{e,0} \lesssim 2.5 \times |E_{b,i}|$. On the other hand, plasmas from Rydberg samples with $n \lesssim 40$ evolve with no significant additional ionization of the remaining atoms once a threshold number of ions has been established. The dominant interaction between the plasma electrons and the Rydberg atoms is one in which the atoms are deexcited, a heating process for electrons that competes with adiabatic cooling to establish an equilibrium where $T_{e,0}$ is determined by their Coulomb coupling parameter, $\Gamma_e \sim 0.01$.

DOI: [10.1103/PhysRevA.97.043401](https://doi.org/10.1103/PhysRevA.97.043401)**I. INTRODUCTION**

The behavior and properties of ultracold neutral plasmas (UNPs) made by direct photoionization of cold atoms in a magneto-optical trap (MOT), first discovered in 1999 [1], are now relatively well understood (see, for instance, Refs. [2,3]). Above the ionization threshold, E_I , conservation of linear momentum in the ionization process dictates that most of the excess photon energy, $\Delta E = h\nu - E_I$, goes to the electron. When the ionizing laser is tuned well above threshold, the initial electron temperature, $T_{e,0}$, is given by $\Delta E = \frac{3}{2} k_B T_{e,0}$. The asymptotic plasma expansion velocity of the plasma is given by

$$v_0 = \sqrt{\frac{k_B(T_{e,0} + T_{\text{ion},0})}{m_{\text{ion}}}}, \quad (1)$$

where m_{ion} is the ion mass. The initial ion temperature, $T_{\text{ion},0}$, is determined largely by the temperature of the parent atoms in the MOT and is typically in the range 0.1–10 mK for UNPs made from noble gas atoms, alkalis, or alkaline earth metals. However, a number of mechanisms rapidly heat both electrons and ions. Specifically, close to threshold, three-body recombination (TBR) heats the electrons and results in minimum $T_{e,0}$ values in the range 30–50 K, and, at high density, threshold lowering (TL) will also affect $T_{e,0}$ [4]. [That is, these mechanisms cause v_0 to be higher than Eq. (1) predicts, based on the $T_{e,0}$ determined by the excess energy of the ionizing photon.] Additionally, the ions are subject to disorder-induced heating (DIH), which heats them up to

~ 1 K in the first few microseconds of the plasma evolution process at higher densities [3,5] but is much less significant in UNPs created in the low-density regime [6,7]. As the plasma expands adiabatically on a time scale of order 10–100 μs , both the electron and ion temperatures fall below the initial values determined by ΔE , TBR, TL, and DIH. Additionally, the Coulomb coupling parameter, Γ_α , increases [2], where

$$\Gamma_\alpha = \frac{e^2}{4\pi\epsilon_0 a_\alpha k_B T_\alpha}, \quad (2)$$

and a_α is the Wigner-Seitz radius for species α (which may be electrons, e , or ions, ion). As a consequence of the competition between adiabatic cooling and TBR, it has been shown that, for typical initial conditions, UNPs tend to equilibrate to $\Gamma_e \sim 0.1$ [8].

UNPs also evolve spontaneously from dense samples of cold Rydberg atoms. Such plasmas (herein termed Rydberg plasmas) are made from cold atoms in a MOT. They were first reported in Refs. [9,10], though a similar phenomenon in dense thermal samples in an atomic beam was observed much earlier [11]. Additionally, Rydberg plasmas have also been created using translationally cool atoms and molecules in a supersonic beam [12,13]. For Rydberg plasmas created in a MOT, it has been shown that dipole interactions between cold (“frozen”) Rydberg atoms play a significant role in the initial ionization [14,15] and black-body radiation (BBR) [16,17], and collisions with hot background Rydberg atoms also contribute [18]. Once a critical electron density threshold is achieved, an avalanche of electron-Rydberg collisions is initiated, and the plasma evolves mediated by the exchange of energy between the Rydberg atoms and the UNP. However, to our knowledge, there have been no extensive experimental investigations of

*duncan.tate@colby.edu

the dependence of the expansion velocity of a Rydberg plasma on density and initial binding energy, $E_{b,i}$.

The ionization processes which initiate Rydberg plasmas, and the effect of the UNP so created on the Rydberg state distribution, have been considered theoretically in a number of papers (see, for example, Refs. [19,20]). However, these papers do not discuss any correlation of the plasma electron temperature with the changing state distributions due to the presence of the daughter UNP. There have also been a theoretical investigation of the feasibility of reaching the strongly coupled regime for the ions in UNPs ($\Gamma_{\text{ion}} \gtrsim 1$) using dipole-blockaded cold Rydberg samples [21] and several experimental studies using optical imaging of Rydberg plasmas of the critical processes during the avalanche regime [22–24]. In particular, in Ref. [22], an electron temperature of 30 ± 10 K was found at the end of the avalanche for a UNP which evolved from $55s_{1/2}$ ^{87}Rb atoms at densities $\lesssim 10^{11} \text{ cm}^{-3}$, while in Ref. [23], temperatures of 26.0 and 48.7 K were found for UNPs from ^{87}Rb samples in the $45s_{1/2}$ and $40d$ states, respectively. However, in both studies, these temperatures were found indirectly from models that describe how the optical depth in absorption imaging of a particular hyperfine component of the $5s_{1/2} \rightarrow 5p_{3/2}$ transition is affected when the $5p_{3/2} \rightarrow n\ell$ transition is excited with narrow bandwidth laser pulses of duration 5–35 [22] and 200 μs [23]. Furthermore, these papers give no information on how the electron temperatures found depend on density or how the interaction of the plasma and the Rydberg atom reservoir affects the Rydberg atoms, and for each paper, only one or two states were investigated. Finally, there has been extensive work done on UNPs which evolve from translationally cold samples of Rydberg NO molecules in a supersonic beam by a group at the University of British Columbia (see Ref. [13] and references therein). Such Rydberg plasmas have significantly more complex behaviors than do atomic UNPs due to additional dynamical pathways available to molecular systems.

This paper reports a systematic experimental and numerical study of the asymptotic expansion velocity of UNPs which evolve from cold Rydberg samples, as a function of the initial binding energy and the initial Rydberg density. From v_0 , we use Eq. (1) to infer a value for $T_{e,0}$ for such plasmas. This “effective initial electron temperature” is a phenomenological parameter which is related to the mean kinetic energy of an ion’s outward velocity late in the plasma evolution. Nevertheless, $T_{e,0}$ is a standard parametrization of the electron thermal energy early in the plasma evolution and allows comparisons to be made with UNPs made by direct photoionization [2]. First, we describe our experiments and the critical results. Then, we discuss our numerical modeling of these systems and how they substantially replicate the experimental findings. The model is then used to gain an intuitive understanding of the interactions between the electrons and the Rydberg reservoir during the plasma evolution process.

II. APPARATUS

Our study concerns UNPs which evolve from cold nd_j ^{85}Rb Rydberg atoms ($24 \leq n \leq 120$). The effective initial electron temperature, $T_{e,0}$, of these UNPs is found by measuring their asymptotic expansion velocity, v_0 , from ion time-of-flight

(TOF) spectra. The Rydberg atoms are created from cold atoms in a MOT which has a maximum atom density of approximately $1 \times 10^{10} \text{ cm}^{-3}$ ($1/\sqrt{e}$ radius $\sigma_0 \approx 400 \mu\text{m}$) and atom temperature $\sim 100 \mu\text{K}$. The atoms are excited to the nd_j states using a narrow-bandwidth pulsed laser system (NBPL) [25]. Excitation of the cold atoms takes place between two parallel high-transparency copper meshes separated by 18.3 mm which may be biased to null out external fields, and we can also apply voltage pulses to selectively field ionize (SFI) Rydberg atoms. (We use SFI in this experiment only to remove atoms excited to Rydberg states from the trap in order to measure the Rydberg atom density as described below.) We monitor the plasma evolution, or the SFI signal, by either observing electrons or ions using a microchannel plate detector (MCP). We achieve Rydberg densities in the range 1×10^7 to $1 \times 10^9 \text{ cm}^{-3}$, which we vary by changing the laser pulse energy. The number of atoms excited is monitored by measuring the 780-nm resonance fluorescence depletion when we apply an SFI pulse immediately after laser excitation [26]. (The SFI pulse has a magnitude which is significantly greater than the classical ionization threshold, $1/16n^{*4}$ in atomic units, where n^* is the effective principal quantum number of the Rydberg state.) The Rydberg atom densities have an absolute uncertainty of a factor of approximately 2 and a relative uncertainty of 20–30%. The NBPL laser beam is unfocused, with a diameter of ≈ 4 mm. This is much larger than the size of our cold atom sample, whose diameter we measure by imaging the 780-nm fluorescence onto a linear diode array. To minimize systematic effects due to laser beam movement (which can affect the geometry of the interaction region relative to the MCP, with consequent impact on the parameters found from fitting the ion TOF signal), we used fixed apertures to define the NBPL beam axis and optimized the position of the MOT atom cloud to this axis.

The field of ion TOF spectroscopy is well developed and exceedingly diverse. In the context of these experiments, the technique is applied to obtain the expansion velocity of a spherically symmetric ion cloud. A similar method has been used in molecular beam UNP experiments by the group at UBC, where the time profile of the ion cloud is observed as a function of plasma evolution time, which is varied by simply moving the detection system longitudinally along the beam [27]. However, when the UNP center-of-mass is stationary, the situation is somewhat more complex, and the principle of the ion TOF technique we use is described in Ref. [28]. After excitation, the cold Rydberg samples evolve to plasma over a period of $\leq 10 \mu\text{s}$, which is negligible in comparison with the overall expansion time of the UNP (100–200 μs). The plasma slowly expands, and we use the MCP to detect plasma ions which exit the field-free interaction region between the meshes. Specifically, the ions we detect are those which leave the interaction region through the left-hand field mesh in Fig. 1 and enter the cylindrical region centered on the z axis whose cross section is defined by the MCP acceptance aperture. Mathematically, the number of ions in this volume of space, N_{out} , is

$$N_{\text{out}} = 2\pi \int_{\theta=0}^{\theta_{\text{max}}} \int_{r=d/\cos\theta}^{\infty} \left[\frac{N_{\text{ion}}}{(2\pi\sigma^2)^{3/2}} e^{-\frac{r^2}{2\sigma^2}} \right] r^2 \sin\theta \, dr \, d\theta, \quad (3)$$

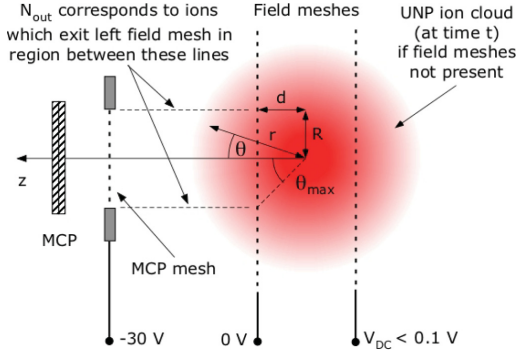


FIG. 1. Schematic of the field meshes and MCP used to obtain the plasma asymptotic expansion velocity from the ion TOF signal. The apparatus is cylindrically symmetric about the z axis. Spherical coordinates r , θ , and ϕ (the azimuthal angle) specify the location relative to the center of the plasma, R is the effective acceptance radius of the MCP, and d is half the field mesh spacing. The angle $\theta_{\max} = \tan^{-1}(R/d)$ defines the effective maximum acceptance angle of the MCP. See text for details. V_{DC} is a small voltage applied to null the effect of external fields in the interaction region between the field meshes.

where the term in square brackets inside the integral is the Gaussian ion density distribution, $\rho_{\text{ion}}(r, t)$ (the total ion number is N_{ion}), r is the distance from the center of the plasma, and t is the time since it was created. The plasma has a characteristic radius $\sigma(t) = \sqrt{\sigma_0^2 + v_0^2 t^2}$, and other quantities are defined in Fig. 1. (The equation has already been integrated with respect to ϕ .)

Our MCP signal is proportional to the ion current, $\frac{dN_{\text{out}}}{dt}$, where N_{out} is given by Eq. (3), and we fit our ion TOF signal using this equation. We thus assume that the part of the UNP that lies between the field meshes is unaffected as the outermost ions exit this region and are accelerated toward the MCP. Since the mesh we use (Buckbee-Mears MC-4) has a transparency of 95% and the electric fields between the meshes, and between the left field mesh in Fig. 1 and the MCP, have magnitudes $\lesssim 0.1$ V/cm and ≈ 10 V/cm respectively, this assumption seems reasonable. Additionally, the use of similar meshes through which electrons or ions pass in imaging or TOF measurements on UNPs has been used extensively in other work, and no significant perturbations due to the meshes have been found (see, for example, Refs. [12, 28, 29]). We assume the ions follow straight line paths parallel to the symmetry axis (the z axis in Fig. 1) between the field mesh and the MCP mesh. While there may be some weak ion lensing effects in this region (discussed below), the maximum ion density here is of order 10^5 cm^{-3} , too low for any significant Coulomb repulsion effects. The ions generally start to arrive at the MCP 30–40 μs after the NBPL pulse, and the MCP signal peaks between 80 and 100 μs , with an overall duration of $\lesssim 400 \mu\text{s}$. Since $\sigma_0 \ll v_0 t$ for all t where the MCP signal is nonzero, we make the substitution $\sigma = v_0 t$. The time dependence of the signal predicted using Eq. (3) depends on only three free parameters: v_0 , N_{ion} , and a geometric factor which depends

on θ_{\max} . The MCP signal we detect depends additionally on an unknown but constant detection conversion factor (i.e., the current output for an ion flux of 1/s), which with N_{ion} affects only the vertical scaling of the detected signal, and a time offset which reflects the flight time of the ions from where they exit the field meshes to the MCP itself. (For all our data, we subtracted off a background signal obtained with the MOT magnetic field turned off, but with the NBPL beam entering the interaction region.) Fitting our data using Eq. (3) and allowing the vertical scaling parameter to float, but with specified offset time and θ_{\max} , enabled us to extract a values for v_0 .

We use these v_0 values to obtain values for $T_{e,0}$ using Eq. (1), making the assumption that $T_{\text{ion},0} \lesssim 1$ K, and is therefore negligible in comparison to $T_{e,0}$. We have carried out extensive calibration of this technique by using it to find v_0 values for UNPs made by photoionizing cold atoms in the limit where $T_{e,0}$ is well above the regime in which TBR is important ($T_{e,0} = 50$ –300 K), and find v_0 to be in agreement with Eq. (1), if we ignore $T_{\text{ion},0}$ and use $\Delta E = \frac{3}{2} k_B T_{e,0}$. The values of $T_{e,0}$ we obtain for Rydberg UNPs are in the range 20–130 K, with an uncertainty of $\sqrt{(10 \text{ K})^2 + (0.1 \times T_{e,0})^2}$. The ion TOF spectra exhibit small systematic differences from Eq. (3), and this makes the v_0 values we obtained sensitive to the time offsets and MCP acceptance angles, which were kept constant in the fits. Our uncertainty estimate, found by fitting selected TOF spectra using a range of different time offsets and MCP acceptance angles, reflects the impact of three systematic effects which are not included in Eq. (3). Specifically, the UNP density profile falls off more sharply than the Gaussian function assumed near the edges [19, 30], and there are variations in the effective acceptance angle of the MCP due to ion lensing effects between the field mesh and the MCP. There is a mesh with voltage -30 V just in front of the MCP, while the field mesh nearest the MCP is grounded. This effectively forms a weak ion lensing system, and will result in a velocity-dependent effective aperture of the MCP. The hydrodynamic velocity of an ion, \vec{u} , is related to its position \vec{r} relative to the center of the plasma by the parameter $\gamma(t)$, where

$$\vec{u}(\vec{r}, t) = \gamma(t) \vec{r} = \frac{v_0^2}{\sigma(t)^2} t \vec{r} \quad (4)$$

[see Ref. [2], Eqs. (24)–(26)]. Because \vec{u} depends on \vec{r} and t , there will be slight variations in the effective acceptance angle of the MCP over the course of the UNP evolution. Finally, during the course of the modeling described below in Sec. IV, we found that UNPs which evolve from cold Rydberg samples take a relatively long time to reach a constant value for v_0 . During the modeling, we found the $m_{\text{ion}} v_0^2 / k_B$ values reached more than 95% of their final values within 40 μs of the plasma creation, and this is less than the time of flight for the first ions we detect in our experiment. Nevertheless, since our fitting routine assumes v_0 is constant, the v_0 values we obtain will be subject to error from this source, too.

III. EXPERIMENTAL RESULTS

Typical results for $T_{e,0}$ are shown in Fig. 2 as a function of the reciprocal of the Rydberg atom spacing, $1/a_R = (4\pi\rho_{R,\text{avg}}/3)^{1/3}$, where $\rho_{R,\text{avg}}$ is the average Rydberg atom density, for different nd states in the range $24 \leq n \leq 120$. The

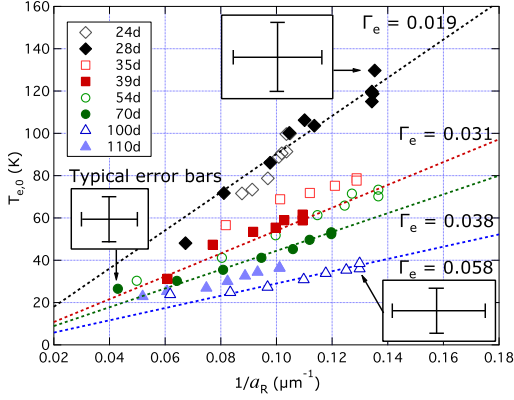


FIG. 2. Graph of $T_{e,0}$ vs $1/a_R$, where a_R is the mean Rydberg atom spacing, for UNPs evolving from cold nd Rb Rydberg samples in the range $24 \leq n \leq 110$. Within the experimental uncertainties, the data for a given Rydberg state are consistent with a straight-line relationship (with y intercepts of zero). The dashed lines are straight-line fits that are constrained to have zero intercepts, and the corresponding Γ_e values are given for 28d, 39d, 70d, and 100d, assuming that a_e , the Wigner-Seitz radius for electrons in the UNP, is equal to a_R . Typical error bars are as shown.

low- $T_{e,0}$, low- $1/a_R$ cutoff ($n = 24$) in the data is determined by the lowest density sample that would spontaneously evolve into a UNP, whereas the high- $T_{e,0}$, high- $1/a_R$ cutoff ($n = 120$) is determined by our maximum achievable density due to the declining oscillator strength of the $5p_{3/2} \rightarrow nd$ transition and the maximum pulse energy available from the NBPL.

There are a number of interesting features in the data shown in Fig. 2. First, within the experimental uncertainties, the results for a single Rydberg state fall on a straight line whose y intercept is zero. The data shown in Fig. 2 therefore provide strong circumstantial evidence that the plasmas which form from a particular nd state have approximately constant initial Γ_e values, regardless of density. Specifically, if we rewrite Eq. (2) for electrons, we see that

$$T_e = \left(\frac{e^2}{4\pi\epsilon_0 k_B} \frac{1}{\Gamma_e} \right) \frac{1}{a_e} = \frac{16.7 \text{ K}\mu\text{m}}{\Gamma_e} \frac{1}{a_e}. \quad (5)$$

Hence, for constant Γ_e , a plot of T_e versus $1/a_e$ will be a straight line. The data in Fig. 2 plot $T_{e,0}$ versus $1/a_R$, and the relationship between the mean Rydberg atom spacing and the Wigner-Seitz radius for the electrons depends on the fraction of Rydberg atoms which ionize, f , as $a_e/a_R = f^{-1/3}$. However, the $f^{-1/3}$ scaling makes a_e/a_R relatively insensitive to the ionization fraction: A variation of f from 0.1 to 0.8 changes a_e/a_R by only a factor of 2. If we assume that $f = 1 \Rightarrow a_e = a_R$, we find that the values of Γ_e vary from 0.02 (28d) to approximately 0.06 (100d). Lines of constant Γ_e using this assumption are shown in Fig. 2 for the 28d, 39d, 70d, and 100d states. (Note that these Γ_e values are characteristic of times early in the plasma evolution, found using the $T_{e,0}$ values inferred from the asymptotic v_0 values.)

The second feature apparent in Fig. 2 is that Γ_e generally increases as the magnitude of the initial binding energy, $E_{b,i}$, decreases, where

$$E_{b,i} = -\frac{e^2}{4\pi\epsilon_0} \frac{1}{2a_0 n^{*2}}, \quad (6)$$

in which a_0 is the Bohr radius and n^* is the effective principal quantum number of the initial nd state, $n^* \approx n - 1.35$. While there is some scatter from a monotonic relationship between $T_{e,0}$ and $|E_{b,i}|$ for fixed $1/a_R$, the scatter between close nd states is within our experimental uncertainties. The data shown in Fig. 2 indicate a significant correlation between $T_{e,0}$ and the initial Rydberg state binding energy, and this suggests that it would be useful to plot the data using the scaled quantities $\tilde{T} = k_B T_{e,0} / |E_{b,i}|$ and $\tilde{a}_e = a_e / 2n^{*2} a_0$. Using this scaling, it can be seen that Eq. (2) for electrons can be expressed as

$$\Gamma_e = \frac{1}{\tilde{a}_e \tilde{T}}, \quad (7)$$

and thus for constant Γ_e , one expects $\tilde{T} \propto 1/\tilde{a}_e$.

To plot our data using Eq. (7) would require values for a_e , which in turn would need accurate measurements of f . In principle, f can be measured at a particular evolution time by applying a sufficiently large negative-voltage SFI pulse and observing the electrons liberated as the UNP is quenched by the leading edge of the pulse and those which arrive later as the SFI pulse field ionizes successively more deeply bound Rydberg states. However, it is hard to do this with any degree of precision unless an accurate measurement is made of the number of free plasma electrons which escape before the SFI pulse is applied, and there is also significant uncertainty due to migration of Rydberg population to deeply bound states which cannot be field ionized. Additionally, f changes during the course of the plasma evolution, and without extensive modeling, choosing the appropriate time to evaluate f would also introduce significant uncertainty. As a consequence of these considerations, we opted to use numerical modeling to obtain values for f , $T_{e,0}$, and other related plasma parameters, as functions of plasma evolution time. From this, we standardized on a specific time during the plasma evolution, $t = 40 \mu\text{s}$, at which to take a snapshot of the evolution that we then compared against the experimental results. The numerical analysis is described below in Sec. IV.

For the moment, given the relative insensitivity of the ratio a_e/a_R on f , we will find it useful to continue using a_R as a proxy for a_e , and the related scaled quantity $\tilde{a}_R = a_R / 2n^{*2} a_0$ as a proxy for \tilde{a}_e . We have therefore plotted \tilde{T} versus $1/\tilde{a}_R$, as shown in Fig. 3. A full discussion of the analysis of this experimental data is described in Sec. IV. First, however, there are a number of significant conclusions that can be drawn from the data shown in Fig. 3. As can be seen, using the scaled quantities \tilde{a}_R and \tilde{T} results in a single universal curve, indicating that the system is behaving in an approximately classical fashion. This is a consequence of general scaling behaviors of processes involving Rydberg atoms, for instance, ionization by collisions with electrons [31] and the relative insignificance of deexcitation by radiative decay, at least for states with $n \geq 40$ [25]. The values of \tilde{T} are all of order unity ($0.2 \lesssim \tilde{T} \lesssim 3$), in line with what one would expect based on

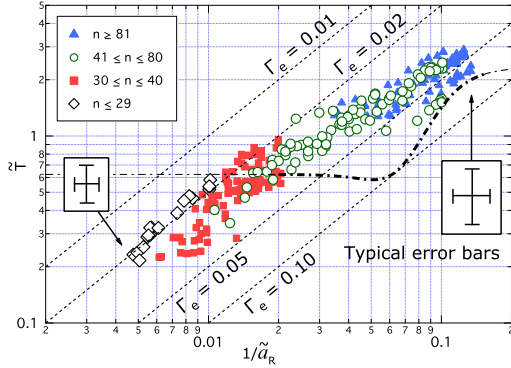


FIG. 3. Graph of experimental \tilde{T} vs $1/\bar{a}_R$ values for UNPs evolving from cold nd Rb Rydberg samples in the range $24 \leq n \leq 120$. The data shown comprise 28 different n values, and for each n , data were obtained for at least six, and up to 20, different densities. We distinguish the data in terms of ranges of n as shown in the legend. (For reference, $n \leq 29$ corresponds to $|E_{b,i}|/k_b > 200$ K; $30 \leq n \leq 40$ to $200 \geq |E_{b,i}|/k_b > 100$ K; $41 \leq n \leq 80$ to $100 \geq |E_{b,i}|/k_b > 25$ K; and $n \geq 81$ to $|E_{b,i}|/k_b \leq 25$ K.) Typical error bars are as shown. Also shown are black dashed lines corresponding to $\Gamma_e = 0.01, 0.02, 0.05$, and 0.1 , found assuming that $a_e = a_R$. The black dash-dotted line is predicted using Eqs. (8)–(12) as described in Sec. IV D for $n > 40$ (the bold section corresponds to the range of final ionization fractions for which the model is valid).

a consideration of the inverse process, TBR in UNPs made by photoionization, for which electrons with energy $k_B T_e$ undergo recombination into states bound by $\sim k_B T_e$ [8,32]. Additionally, \tilde{T} is larger for high- n states than for low- n states, and has an almost linear dependence on $1/\bar{a}_R$.

As with Fig. 2, in Fig. 3 the ratio of the Wigner-Seitz radius for the electrons in the UNP to the mean Rydberg atom separation varies with f over the range of \bar{a}_R values. However, theoretical results given in Refs. [8,19,20] show that a maximum of $f \approx 0.7$ of the Rydberg atoms ionize during the avalanche for principal quantum numbers in the range $n = 45$ – 70 and densities of 10^8 – 10^9 cm $^{-3}$ (our own analysis, described in Sec. IV, gives a maximum final ionization fraction of $f_f = 0.83$ for $n = 120$). This suggests that for the data with $1/\bar{a}_R > 0.1$, $\tilde{T} > 2$ in Fig. 3, $1/\bar{a}_e = f^{1/3}/\bar{a}_R \approx 0.9/\bar{a}_R$. For these data points, the values of $\Gamma_e \approx 0.06$ found assuming $a_e = a_R$ are therefore quite accurate. On the other hand, in the low- $1/\bar{a}_R$, low- \tilde{T} part of the graph, the data points will be skewed to the left relative to those in Fig. 3 when plotted versus $1/\bar{a}_e$. For instance, the lowest point on the graph in Fig. 3 is ($1/\bar{a}_R \approx 0.005$, $\tilde{T} \approx 0.2$). This point would correspond to ($1/\bar{a}_e \approx 0.001$, $\tilde{T} \approx 0.2$) if $f = 0.01$, giving $\Gamma_e \approx 0.005$.

The range of Γ_e values we obtain are reasonably comparable with those reported in other experiments using different methods. Specifically, the NIST group found $0.02 < \Gamma_e < 0.08$ [33] and $\Gamma_e = 0.13$ [34] for Xe plasmas made by photoionization, using electron spilling, and measurement of TBR rates, respectively. Gupta *et al.* found $\Gamma_e \lesssim 0.1$ for Sr plasmas made by photoinization with $T_{e,0} > 45$ K, $\rho_{\text{ion,avg}} < 4.0 \times 10^9$ cm $^{-3}$

using the method of laser velocimetry of the Sr^+ resonance line but found larger Γ_e values at lower initial temperature and higher density [35]. Additionally, we have compared our Γ_e values with those obtained from a Monte Carlo model provided to us by Robicheaux [8,19]. While the model analyzes UNPs made by photoinization, rather than those which evolve from Rydberg samples, it is to be expected that there should be a reasonably smooth variation in the plasma properties in the region of the ionization limit. When we simulate this system using density and size parameters comparable to our experiment $\rho_{R,\text{avg}} \sim 10^8$ cm $^{-3}$ and $\sigma_0 \approx 400$ μm , we find Γ_e values in the range from 0.01 ($T_{e,0} = 140$ K) to 0.09 ($T_{e,0} = 20$ K). On the other hand, UNPs which evolve from Rydberg states of cold NO molecules in a supersonic beam have been reported to have $T_e \approx 7$ K at a density such that $a_e = 360$ nm, implying $\Gamma_e \approx 7$ [36].

IV. NUMERICAL MODELING

A. Approach and initial conditions

In order to understand what the data shown in Fig. 3 say about how UNPs which evolve from cold Rydberg samples behave, and in particular, what determines the effective initial electron temperature, $T_{e,0}$, we have carried out extensive modeling of the interaction between a cold plasma and a coexisting reservoir of Rydberg atoms. Specifically, we have used a program provided to us by Robicheaux, which uses the Monte Carlo method to calculate the effects of electron-Rydberg collisions, TBR, and other interactions on the plasma evolution process [8,19]. The initial conditions are specified numbers of ions, electrons with a specific temperature, and Rydberg atoms in a specific nd state. The Rydberg atoms are distributed randomly within a Gaussian envelope with an initial characteristic radius σ_0 . Similarly, the initial electron and ion density distributions are Gaussian with initial radius σ_0 . For each electron-Rydberg collision, the probabilities for excitation, deexcitation, and ionization are compared with randomly generated probabilities, and the effect of the successful outcome is accounted for in terms of the change in the number of ions, free electrons, and neutral atoms, the energy of each atom, and the mean energy of the electrons. The effects of electron-ion collisions on the ion number, Rydberg atom number, their state distributions, positions, and velocities are tracked, as well as the effect of radiative decay of the Rydberg atoms. For each time iteration, the differential equations which describe the global plasma parameters [see Ref. [19], Eqs. (12)] are solved numerically using the relevant particle numbers and energies. The program does not model how a cold Rydberg sample evolves into a UNP; rather, we use it to find how a reservoir of Rydberg atoms affects the evolution of a coexisting UNP. Hence, we are effectively modeling the evolution of a Rydberg plasma from the onset of the avalanche regime, and we run the simulation until a final time of 40 μs later.

In understanding this approach to modeling of Rydberg plasmas, it is useful to make an analogy with how the electron temperature evolves in UNPs made by direct photoionization. Immediately after the ionization laser pulse, a plasma forms if there is sufficient ion density to trap the electrons. If the densities are high and the electron temperature T_e is low,

TBR, with a rate which scales as $\rho_e^2 \rho_{\text{ion}} T_e^{-9/2}$ (ρ_e and ρ_{ion} are the electron and ion density, respectively), heats the plasma electrons and creates bound Rydberg atoms. The TBR phase ends due to the $T_e^{-9/2}$ rate dependence: the remaining electrons are heated by TBR, which in turn reduces the TBR rate until it becomes comparable to the rate of electron replenishment due to ionizing electron-Rydberg collisions [34]. Thereafter, the plasma expands, and the electrons cool adiabatically, though a small amount of electron heating occurs due to electron-Rydberg collisions driving the atoms to more deeply bound states, and TBR, which continues at a low rate because T_e falls throughout the expansion [34]. The asymptotic plasma expansion velocity, v_0 , is described by Eq. (1), where $T_{e,0}$ is the electron temperature resulting from the ionizing photon's excess energy, heat added during the TBR phase, and the small amount of heating or cooling which happens after the TBR phase ends [32,37].

For Rydberg plasmas, the period which corresponds to the TBR phase is the avalanche regime, where the rates of collisions between electrons and Rydberg atoms and between electrons and ions are high. During this phase, for $n \geq 40$, anywhere from a few percent to more than 80% of the atoms ionize, while the remaining bound atoms are scattered to more deeply bound states. However, there will be significant interaction between the electrons and Rydberg atoms throughout the evolution of a Rydberg plasma, given that there is a much larger reservoir of Rydberg atoms than in a photoionization-initiated UNP [20]. The avalanche regime is thus unlikely to have as distinct an end point as the TBR phase in conventional UNPs. As noted above in Sec. II, our simulations showed that v_0 continued to increase for several tens of μs into the plasma evolution. Collisions between electrons and the Rydberg atoms drive the atoms to more deeply bound states, and the energy so liberated accelerates the plasma expansion [8]. We chose an end point for the simulations of 40 μs after the plasma was created as a reasonable compromise for comparison with the experimental results. At this time, we found that the quantity $T_{e,0} = m_{\text{ion}} v_0^2 / k_B$ attained at least 95% of the value it would have reached for much longer simulation times. In a conventional UNP made by photoionization, and which experiences no TBR heating, $T_{e,0}$ would be the actual initial electron temperature; however, in our case, it is just a useful measure of the net thermal energy transferred from other degrees of freedom into the outward expansion of the plasma.

For the moment, we will concentrate on plasmas which evolve from Rydberg atoms with $n \gtrsim 40$. (Below $n = 40$, we find that there is in general very little additional ionization after the threshold condition is reached. This regime is discussed more extensively in Sec. IV E.) With the picture described in the previous paragraph in mind, we consider the initial condition to be the beginning of the avalanche regime. At this time, when the initial ionization fraction is f_i , there are $N_{R,i} = (1 - f_i)N$ Rydberg atoms in a specific nd state with binding energy $E_{b,i}$ which interact with $N_{\text{ion},i} = f_i N$ ions and $N_{e,i} = N_{\text{ion},i}$ electrons with a specified initial temperature, $T_{e,i}$. (The ions and Rydberg atoms are assumed to be stationary at this time.) The final condition is the end of the simulation, 40 μs after the plasma is created. At this time, the ionization fraction is $f_f = N_{\text{ion},f} / N$, the mean Rydberg binding energy is $\bar{E}_{b,f}$,

and the electron temperature is $T_{e,f}$. Additionally, thermal and binding energies have been converted to kinetic energy of the ions. When the plasma expansion velocity is v_0 , the mean ion kinetic energy is $(3/2) m_{\text{ion}} v_0^2$ (see Sec. IV D). We obtain the plasma expansion velocity for each time step in the evolution using the characteristic radius of the UNP, $\sigma(t)$, which is one of the program outputs, and the equation $\sigma(t) = \sqrt{\sigma_0^2 + v_0^2 t^2}$. The value of v_0 for the last time iteration before the simulations end at 40 μs is the one we relate back to the effective initial electron temperature, $T_{e,0}$, using Eq. (1), again assuming that $T_{\text{ion},0} = 0$.

Our assumptions are crude in that they do not consider that the initial ionization process which seeds the plasma probably leads to a distribution of electron energies and redistributes some of the Rydberg atoms to states different from that excited by the laser [38,39]. Additionally, cold dipole collisions are faster for close atom pairs, causing a Rydberg atom distribution different from one which is random within a Gaussian envelope [40]. However, these affect only a fraction $\sim f_i$ of the Rydberg atoms, and the net effect of neglecting these deviations at the end of the simulation is probably negligible. While we were unable to test this hypothesis with regard to the reduction in the number of close atom pairs, the simulation results were not significantly dependent on the value of $T_{e,i}$ used and varied only weakly with $E_{b,i}$.

While the quantities f_i and $T_{e,i}$ are presumably determined by the dominant initial ionization mechanism, they are not quantities which we can measure and they are not predicted by the program we use. Instead, for a given nd state, we have run the models with $f_i = 0.5, 0.1, 0.01, 0.001$, and $T_{e,i} = 5$ ($n \geq 50$ only), 10, 25 (all n), and 50 K ($n \leq 40$ only). It turned out that the results for almost all the Rydberg states we investigated were substantially independent of the f_i and $T_{e,i}$ values chosen. This makes sense: Given the large number of Rydberg atoms relative to the number of seed electrons, after only a few electron-atom collisions, the properties of the free electrons are determined by the Rydberg reservoir much more than by the initial electron temperature and density. In addition, all the simulation results for the relationship between \bar{T} and $1/\bar{a}_R$ closely agreed with what we measured, as can be seen in Fig. 4. The f_i and $T_{e,i}$ values we used in our simulations are reasonable based the initial ionization mechanisms [11,16–20,38] and the number of ions needed to establish a potential well of depth $\sim |E_{b,i}|$ and radius σ_0 [1]. We will therefore consider the insensitivity of the simulation results to specific f_i and $T_{e,i}$ values and their agreement with the experimental results as a sufficient justification for our choice of initial parameters.

For each nd , f_i , $T_{e,i}$ combination, we use average total densities (atoms + ions) $N / (4\pi\sigma_0^2)^{3/2} = 1 \times 10^7, 2 \times 10^7, 3 \times 10^7, 5 \times 10^7, 1 \times 10^8, 2 \times 10^8$, and $3 \times 10^8 \text{ cm}^{-3}$, and an initial plasma radius $\sigma_0 = 212 \text{ }\mu\text{m}$. (The maximum density and the σ_0 value we use are determined by available computing power.) The plasmas evolve for 40 μs , at which time we evaluate $T_{e,0}$ and f_f , as well as $|\bar{E}_{b,f}|$. This latter quantity is found by averaging the energies of all the neutral atoms with $n \geq 5$; however, the fraction of atoms which end up below $n = 5$ is significant only for initial nd states with $n \leq 35$. (States with $n < 5$ are would be inaccessible for Rb if

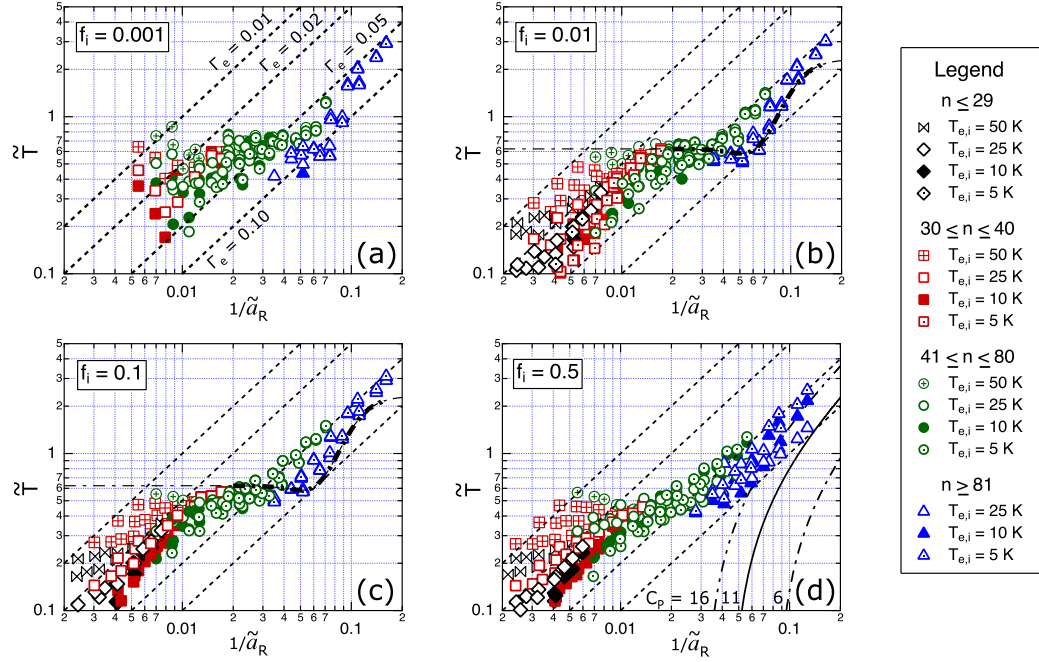


FIG. 4. Results of numerical modeling for \tilde{T} vs $1/\tilde{a}_R$ for UNPs evolving from nd cold Rb Rydberg samples in the range $24 \leq n \leq 120$. (a) $f_i = 10^{-3}$; (b) $f_i = 10^{-2}$; (c) $f_i = 10^{-1}$; and (d) $f_i = 0.5$. We distinguish the data in terms of different n (initial binding energy) ranges and $T_{e,i}$ values as shown in the legend. (For reference, $n \leq 29$ corresponds to $|E_{b,i}|/k_b > 200$ K; $30 \leq n \leq 40$ to $200 \geq |E_{b,i}|/k_b > 100$ K; $41 \leq n \leq 80$ to $100 \geq |E_{b,i}|/k_b > 25$ K; and $n \geq 81$ to $|E_{b,i}|/k_b \leq 25$ K.) Where the 10 and 25 K data points appear to be missing, they lie underneath the corresponding 5 K symbol. The axes have the same range as those of the graph shown in Fig. 3. The black $-\cdot-$ line in panels (b) and (c) is predicted using Eqs. (8)–(12) as described in Sec. IV D for $n > 40$ (the bold section corresponds to the range of final ionization fractions for which the model is valid, $1.5 \times f_i \leq f_f \leq 0.83$). Also shown are lines corresponding to $\Gamma_e = 0.01, 0.02, 0.05$, and 0.1 , found assuming that $a_e = a_R$, with the values of Γ_e for each shown in panel (a). In addition, (d) shows parameter space limits due to threshold lowering for $C_p = 6$ (black, $---$), $C_p = 11$ (black solid line), and $C_p = 16$ (black, $-\cdot-$); see Sec. IV D for details.

the calculation was fully quantum mechanical. However, the model is semiclassical, and the $n < 5$ criterion matters only in that these atoms are removed from the system being modeled [19]. Practically, even atoms significantly above $n = 5$ have very little impact on the plasma dynamics, given their high radiative decay rates and small geometric cross sections.)

B. Results of modeling: \tilde{T} versus $1/\tilde{a}_R$

The results of the analysis described above for the behavior of \tilde{T} versus $1/\tilde{a}_R$ are shown in Fig. 4. As can be seen, for one particular f_i value, there is substantial agreement of the results for different $T_{e,i}$ values for $n > 40$. On the other hand, for $n \lesssim 40$, higher $T_{e,i}$ (50 K) values result in significantly higher \tilde{T} values than for $T_{e,i} = 5, 10$, and 25 K, which give consistent \tilde{T} values. This regime is discussed in Sec. IV E.

In comparing the graphs with different initial ionization fractions, it can be seen that the relationship between \tilde{T} and $1/\tilde{a}_R$ is substantially independent of the value of f_i . The agreement of the simulations using different f_i is strongest for $n > 40$, but even for $n \lesssim 40$ and $T_{e,i} = 10$ K and 25 K,

there is good agreement of the results. For $f_i = 10^{-3}$, we were not able to obtain as many results as for the other f_i values. Many of these simulations failed due to insufficient electron and ion densities to sustain a plasma. Given the instability of the $f_i = 10^{-3}$ simulations, and the low likelihood that a situation where $f_i = 0.5$ would arise, much of the discussion below concentrates on $f_i = 10^{-1}$ and $f_i = 10^{-2}$.

Comparing the experimental data in Fig. 3 with the results of the modeling shown in Fig. 4, there is strong qualitative and quantitative agreement. The end points of the range of $(1/\tilde{a}_R, \tilde{T})$ coordinates, anchored at the low- \tilde{T} end by the $24d$ data and on the high- \tilde{T} end by $120d$, match reasonably well, and the range of Γ_e values (using the proxy $\tilde{a}_e = \tilde{a}_R$) is similar. On the other hand, there are significant differences between the predictions of the model, and the experimental results. First, the $f_i = 10^{-1}$ and 10^{-2} simulations exhibit a weak plateau where $\tilde{T} \approx 0.6$ for $0.01 \lesssim 1/\tilde{a}_R \lesssim 0.03$, whereas in the experimental data, there is no evidence of such a feature. (On the other hand, the plateau behavior is limited to states with $n \geq 80$, and the simulations for $n < 80$ are actually very similar to the experimental results.) Additionally, the range of $(1/\tilde{a}_R, \tilde{T})$

FOREST, LI, WARD, GOODSELL, AND TATE

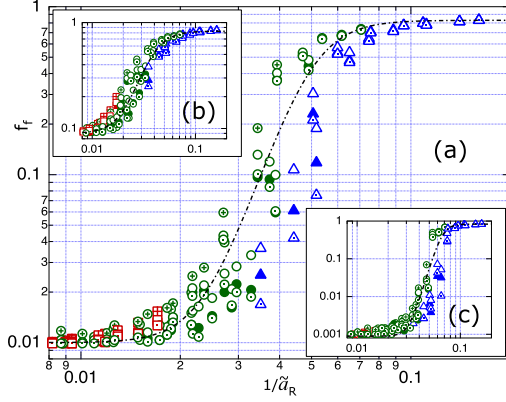
PHYSICAL REVIEW A **97**, 043401 (2018)

FIG. 5. Results of numerical modeling for f_f vs $1/\bar{a}_R$ for UNPs evolving from cold nd Rb Rydberg samples in the range $24 \leq n \leq 120$. (a) $f_i = 10^{-2}$; insets (b) $f_i = 10^{-1}$ and (c) $f_i = 10^{-3}$. We distinguish the data in terms of ranges of n and $T_{e,i}$ using the same scheme as in Fig. 4. The black $- \cdot -$ lines are a simple heuristic relationship given by Eq. (8).

values exhibited by a given n state are generally higher for the experimental data than in the simulations. This discrepancy is primarily caused by the difference in the densities used in the simulations from what was achieved in the experiment. Consequently, the upper and lower bounds of the range of $1/\bar{a}_R$ values were approximately 50% higher in the simulations than in the experiment. Additionally, it is likely that the difference in σ_0 values (212 μm in the simulations, 400 μm in the experiment) contributes to this difference: In our simulations of UNPs created by direct photoionization, we found that v_0 increased with smaller σ_0 values for low $T_{e,0}$ where TBR is significant (the other conditions were kept unchanged).

C. Evolution behavior of a Rydberg plasma

The similarity of the curves shown in Figs. 4(a), 4(b) and 4(c), and to a lesser extent, 4(d), for vastly different f_i and for all initial $T_{e,i}$ in the region $1/\bar{a}_R > 0.02$ ($n \gtrsim 40$), and their similarity to the experimental data shown in Fig. 3, is a significant result. Basically, it suggests two conclusions. The first is that such Rydberg plasmas, once they reach threshold, evolve in a manner which is independent of the initial plasma seeding mechanism. As noted above, this is because the electron temperature and density and the Rydberg state distribution all change rapidly due to the high electron-Rydberg collision rate at the onset of the avalanche. The second conclusion suggested by Figs. 4(a), 4(b) and 4(c) is that for $1/\bar{a}_R > 0.02$, $T_{e,0}$ for the UNP must be intimately related to the final ionization fraction, f_f . To test this hypothesis, we have looked at how f_f depends on $1/\bar{a}_R$ for $f_i = 0.1$, 0.01, and 0.001. These results are shown in Fig. 5. As can be seen, the final ionization fraction, f_f , remains smaller than twice the initial value unless $1/\bar{a}_R \gtrsim 0.02$, and this onset seems to correlate with the rise in \bar{T} seen at the same $1/\bar{a}_R$ in Fig. 4. However, the ionization fraction then rises rapidly, reaching $f_f = 0.50$ between $1/\bar{a}_R = 0.04$

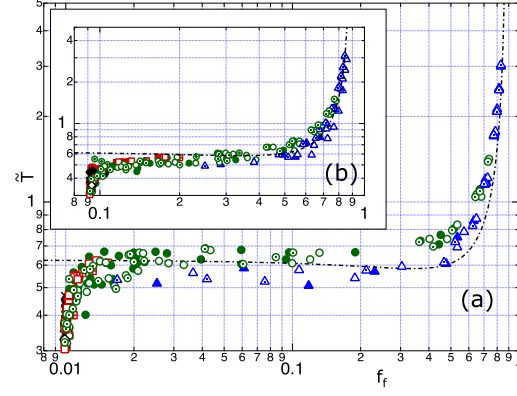


FIG. 6. (a) Results of numerical modeling for \bar{T} vs f_f , for $f_i = 0.01$; inset (b), for $f_i = 0.1$. We distinguish the data in terms of ranges of n and $T_{e,i}$ using the same scheme as in Fig. 4. The black $- \cdot -$ lines are obtained using Eqs. (9) and (12) as described in Sec. IV D and Eq. (12).

and 0.07, and saturates at $f_f \approx 0.83$ regardless of f_i . There is significant variation in f_f values for different $T_{e,i}$ and different $|E_{b,i}|$ in the transition region; however, regardless of these two parameters, the transition from low to high f_f occurs in a well-defined range of $1/\bar{a}_R$ values, and the range varies only slightly with f_i . Additionally, the region where $f_f/f_i \geq 2$ is exhibited only for initial states with $n > 40$, and for all initial states with $n \leq 40$, the number of Rydberg atoms which ionize during the avalanche is very low.

We have found a simple heuristic relationship between f_f and $1/\bar{a}_R$ which describes the gross features of the variation of f_f with $1/\bar{a}_R$:

$$f_f = f_i + (0.83 - f_i) \frac{k/\bar{a}_R^m}{1 + k/\bar{a}_R^m}. \quad (8)$$

Values of k and m which give a reasonable description to the data shown in Fig. 5 are $f_i = 0.1$, $k = 5.4 \times 10^5$, and $m = 4$; $f_i = 0.01$, $k = 6.6 \times 10^7$, and $m = 6$; and $f_i = 0.001$, $k = 3.6 \times 10^{10}$, and $m = 9$. These curves are shown in Fig. 5. As can be seen, Eq. (8) does not describe well the $T_{e,i}$ - and $|E_{b,i}|$ -dependent variations in the transition region, nor does it work well when $f_f \approx f_i$. However, it is a useful relation which we will use in Sec. IV D.

Comparing the results shown in Figs. 4 and 5 in the region $1/\bar{a}_R > 0.02$, we see that f_f rises rapidly with increasing $1/\bar{a}_R$, and \bar{T} shows a marked increase also. There is significant scatter in the dependence of both f_f and \bar{T} on $1/\bar{a}_R$ for $0.02 \leq 1/\bar{a}_R \leq 0.1$, but the scatter is markedly less for both f_f and \bar{T} in the region $1/\bar{a}_R > 0.1$. This suggests that there is a strong correlation between \bar{T} and f_f , and the scatter of \bar{T} versus $1/\bar{a}_R$ in Fig. 4 is related to the scatter of f_f versus $1/\bar{a}_R$ in Fig. 5. To test this relationship, we looked at the dependencies of \bar{T} and the parameter $\beta \equiv |\bar{E}_{b,f}|/k_B T_{e,0}$ on f_f , where $|\bar{E}_{b,f}|$ is the average value of the binding energies of all atoms with $n > 5$ after 40 μs of plasma evolution time. These graphs are shown in Figs. 6 and 7. As can be seen, the hypothesis that there

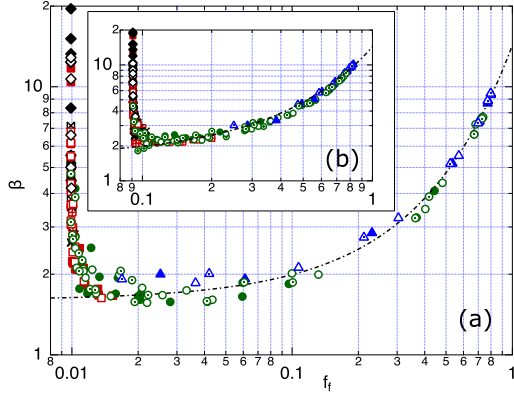


FIG. 7. (a) Results of numerical modeling for β vs f_f , for $f_i = 0.01$; inset (b), for $f_i = 0.1$. We distinguish the data in terms of ranges of n and $T_{e,i}$ using the same scheme as in Fig. 4. The black $-\cdot-$ lines are the heuristic $\beta(f_f)$ given by Eq. (9).

are well-defined relationships between \tilde{T} and f_f and between β and f_f is correct. This makes sense, since \tilde{T} , β , and f_f are all determined by electron-Rydberg collisions. As the number of collisions increases, the degree of ionization is greater and the more energy is transferred from the Rydberg atoms to the plasma expansion.

We have used the data in Fig. 7 to find a simple heuristic relationship between β and f_f . That relationship, which works well for both $f_i = 0.1$ and 0.01 provided that $f_f \gtrsim 2 \times f_i$, is

$$\beta = 1.60 e^{2.19 f_f}. \quad (9)$$

Equation (9) is plotted along with the data in Fig. 7 (the black $-\cdot-$ lines). For low f_f ($f_i < f_f \lesssim 0.3$), β is in the range $1.6 < \beta < 3$, but as f_f rises to its maximum value $\beta \rightarrow 10$. The high- β limit is reached only for $n \gtrsim 100$, and corresponds to the maximum possible $f_f \approx 0.83$. At this point, for every six Rydberg atoms in the initial sample, five have ionized. To maintain the energy balance, the one remaining neutral atom must be much more deeply bound than the initial state, $|\tilde{E}_{b,f}| \geq 6 \times |E_{b,i}|$. This limit is analogous to what has been found for low- $T_{e,0}$ UNPs made by photoionization, where the Rydberg energy states formed by TBR are more deeply bound than for higher $T_{e,0}$ plasmas. Low- $T_{e,0}$ photoionization-initiated UNPs and UNPs which evolve from Rydberg states with low $|E_{b,i}|$ expand slowly, and thus there is more time for electron-Rydberg collisions, which primarily lead to deexcitation of the atoms, to occur [19,32].

D. The effective initial electron temperature of an ultracold Rydberg plasma when $n > 40$

We show here that the connection between \tilde{T} and β is a consequence of energy conservation in the plasma evolution. It has been shown in numerous theoretical studies that there exists a bottleneck energy, E_{bn} , of the Rydberg state distribution for atoms in equilibrium with a plasma with electron temperature T_e [19,41–44]. Specifically, $E_{bn} \approx 4k_B T_e$, and Rydberg states

with binding energy $|E_b| < E_{bn}$ will eventually ionize due to electron collisions, while those with $|E_b| > E_{bn}$ will be deexcited to states with lower n which will eventually decay radiatively to the ground state. The seed electrons which result from BBR photoionization [16,17], cold dipole-dipole collisions [38], or by hot-cold Rydberg collisions [11] all have distributions such that a significant fraction will have energies that are greater than $|E_{b,i}|/4$. This corresponds to the situation where the initial electron temperature $T_{e,i} > |E_{b,i}|/4k_B$, and thus the electron temperature is more than sufficient at the beginning of the avalanche to ionize the Rydberg atoms in the original state, as well as many of the partner atoms deexcited by cold dipole collisions [38], because $E_{b,i}$ is above the bottleneck energy characteristic of a plasma with electron temperature $T_{e,i}$. As the plasma evolves, the interplay of electron-Rydberg exciting, deexciting, and ionizing collisions and recombining maintains the energy balance in the evolution so that the magnitude of the average binding energy of the un-ionized atoms increases. The energy so liberated drives the plasma expansion so that the UNP achieves a final expansion velocity v_0 .

We can verify this picture by looking at what energy conservation predicts about the relationship of \tilde{T} , β , and f_f . Specifically, if we ignore the energy added to the system by BBR and hot-cold Rydberg collisions, the initial energy of the system is

$$E_i = -(1 - f_i)N|E_{b,i}| + f_i N \frac{3}{2} k_B T_{e,i}, \quad (10)$$

where N is the total number of atoms and ions. (We neglect the thermal energy of the ions; as discussed in the introduction, $T_{ion,0} \lesssim 1$ K, and the subsequent adiabatic expansion causes the ion temperature to decrease further.) The final energy of the system is

$$E_f = -(1 - f_f)N|\tilde{E}_{b,f}| + f_f N \frac{3}{2} k_B T_{e,f} + f_f N \frac{3}{2} m_{ion} v_0^2 \sigma^2 \quad (11)$$

[see Ref. [2], Eq. (31e)]. The last term is the kinetic energy contained in the radial expansion of the ions (this is obtained by averaging the quantity $(1/2)m_{ion}|\vec{u}|^2$, where \vec{u} and $\gamma(t)$ are given by Eq. (4), over the density distribution of the ions [2,19]). For times late in the plasma evolution, we can neglect $T_{e,f}$ because of adiabatic cooling. (In the simulations, $T_{e,f}$ was usually ≤ 2 K, and the maximum value we observed was 4 K.) We also make the approximation $m_{ion} \gamma^2 \sigma^2 \approx m_{ion} v_0^2 = k_B T_{e,0}$ which is valid for $v_0 t \gg \sigma_0$ [see Eq. (4)].

Equating the initial and final energies, and using $|\tilde{E}_{b,f}| = \beta k_B T_{e,0}$, we obtain the following relationship

$$\tilde{T} = \frac{k_B T_{e,0}}{|E_{b,i}|} = \frac{\left[1 - \left(1 + \frac{3}{2} \frac{k_B T_{e,i}}{|E_{b,i}|}\right) f_i\right]}{\left[(1 - f_f)\beta - \frac{3}{2} f_f\right]}. \quad (12)$$

For $f_i = 0.1$ the term in the numerator differs significantly from unity, and lies in the range 0.57 (for $T_{e,i} = 25$ K and $n = 120$) to 0.90 (the low n limit). For $f_i = 0.01$, it lies in the range 0.96–0.99. We will ignore this dependence of \tilde{T} on $T_{e,i}$ and $|E_{b,i}|$ and set the numerator to unity, which for $f_i = 0.1$ means that the \tilde{T} values obtained are significant overestimates at high n , though for low n they are good to within 20%. For $f_i = 0.01$, the effect of setting the numerator equal to unity is negligible.

We can now test the thesis that \tilde{T} and β are related by energy conservation. Specifically, we have substituted Eq. (9) into Eq. (12) (with the numerator equal to unity), and this curve is plotted with the numerical data in Fig. 6 (the black $-\cdot-$ lines). As can be seen, the agreement of the numerical data with the prediction based on Eqs. (9) and (12) is very good. We can also understand why there are systematic differences between the heuristic and the numerical results. First, the effect of approximating the numerator to unity in Eq. (12) can clearly be seen in Fig. 6(b) for $f_i = 0.1$: Almost all the simulation data points lie below the heuristic, by $\lesssim 20\%$ for $f_f \leq 0.4$, but by significantly more for $f_f \geq 0.6$, as expected. On the other hand, this difference is much less apparent for $f_i = 0.01$ in Fig. 6(a). The second difference is that for both $f_i = 0.01$ and 0.1 , many data points have \tilde{T} values which are greater than the heuristic predicts in the region $f_f \geq 0.4$. This is a manifestation of the fact that Eq. (12) does not consider the kinetic energy of the Rydberg atoms. Since the atoms are assumed to be initially stationary in the simulations, the only atoms with significant kinetic energy at $40 \mu\text{s}$ will be the ones formed by recombination of electrons with ions which have already acquired a significant outward velocity. In Ref. [20], it is argued that during the expansion, a given Rydberg atom will ionize and recombine many times during the evolution of a Rydberg UNP. Consequently, all of the atoms are essentially dragged along by the plasma, and there should therefore be an additional term in the final energy that is $\lesssim (1 - f_f) N (3/2) m_{\text{ion}} v_0^2$, equivalent to $\lesssim (1 - f_f) N (3/2) k_B T_{e,0}$. This affects the $-(3/2) f_f$ term in the denominator of Eq. (12), and if the Rydberg atoms have the same final velocity distribution as the ions, this term becomes $-(3/2)$, leading to \tilde{T} values which are higher than Eq. (12) predicts. There is no simple relationship we can use to estimate the amount of kinetic energy the Rydberg atoms acquire during the expansion, other than the upper limit, which would correspond to $\tilde{T} \approx 5$ at $f_f = 0.83$ [i.e., replacing $-(3/2) f_f$ with $-(3/2)$ in Eq. (12)]. However, the effect will only influence \tilde{T} values where f_f is significant ($f_f \gtrsim 0.1$, say); if there is not much ionization, there can be few recombination events that result in moving Rydberg atoms. Accounting for the Rydberg atom kinetic energy, the \tilde{T} values could be as much as twice those estimated using Eq. (12) in this region.

We point out in passing that our β and \tilde{T} values are consistent with the theoretical analysis reported in Ref. [20]. While this paper reports only values for ionization fractions and Rydberg state distributions as functions of time when an $n = 70$ state is initially excited, and does not give the corresponding information about the electron temperature, there is enough information in Fig. 3 in Ref. [20] to extract a value for $\beta\tilde{T}$. Specifically, at an evolution time of $25 \mu\text{s}$, Pohl *et al.* found $|\tilde{E}_{b,f}|/|E_{b,i}| = \beta k_B T_{e,0}/|E_{b,i}| = \beta\tilde{T} \approx 8$ when $f_f \approx 0.7$ and $\rho_{\text{avg}} \approx 5 \times 10^9 \text{ cm}^{-3}$. While this density is significantly higher than the one used in our analysis, using Figs. 6 and 7, we obtain $\beta \approx 7.5$ and $\tilde{T} \approx 0.9$, giving a value for $\beta\tilde{T} \approx 7$ when $f_f = 0.7$. In addition, there is agreement with the experiment reported in Ref. [22], where they found $\tilde{T} = 0.6 \pm 0.2$, though those reported in Ref. [23], $\tilde{T} = 0.29$ and 0.46 for plasmas from $45\text{s}_{1/2}$ and $40d$ respectively, are somewhat lower than the minimum value of 0.6 that we get from Eq. (12) using the minimum β value consistent with Fig. 7. On the other hand, the work reported in Ref. [22] claims

a value of $f_f \sim 1$, and for Ref. [23], it was likely similar. For such high f_f , our analysis suggests $\tilde{T} \approx 2.5$. However, both experiments used optical dipole traps which give small σ_0 and make high densities possible, leading to long-lived plasmas ($\lesssim 400 \mu\text{s}$ in [23]). Additionally, both experiments excited the $\text{Rb } 5p_{3/2} \rightarrow n\ell$ transitions for much longer time durations (several μs to $200 \mu\text{s}$) than we do ($\sim 5 \text{ ns}$). The fact that the Rydberg state population changes during the plasma evolution due to this replenishment, and not just as a consequence of the interaction between the plasma and the Rydberg atoms, likely makes the dynamical behaviors seen in Refs. [22,23] significantly different than ours.

We have also used the heuristic relationship between f_f and $1/\bar{a}_R$ described by Eq. (8), and Eq. (12) to model the dependence of \tilde{T} on $1/\bar{a}_R$. Specifically, we used the constants for the condition $f_i = 0.01$ in Eq. (8), and this curve is shown in Figs. 3, 4(b), and 4(c). (The part of the curve denoted by the bold line in the figures corresponds to final ionization fractions for which the heuristics are reasonably accurate representations of the numerical results, i.e., the range $2 \times f_i \leq f_f \leq 0.83$.) The differences in the f_f versus $1/\bar{a}_R$ curves for $f_i = 0.1$ and 0.01 affect only how \tilde{T} changes with $1/\bar{a}_R$ in the region above $1/\bar{a}_R = 0.04$.

In the experimental data shown in Fig. 3, we see that \tilde{T} varies much more gently with $1/\bar{a}_R$ for states with $n > 40$ than the heuristic curve predicts [i.e., from Eq. (12), using Eqs. (8) and (9)], and there is no evidence for a plateau in the experimental result. While the “end points” of $(1/\bar{a}_R, \tilde{T}) \approx (0.02, 0.7)$ and $\approx (0.12, 2.5)$ agree, the experimental \tilde{T} values between these limits are significantly higher than those given by the heuristic. This difference seems to have two primary causes. First, as noted above, Eq. (12) does not account for the kinetic energy of the Rydberg atoms. If this effect were to be included in Eq. (12), the \tilde{T} values predicted would be higher in the range of $1/\bar{a}_R$ where the final ionization fraction is significant. This is exactly the behavior we see in the data, as well as in many of the numerical simulations in Fig. 4. Second, as can be seen in Fig. 6, \tilde{T} does not rise above a value of 1.6 (the $f_f \rightarrow 0$ limit) until $f_f \approx 0.5$. Using Fig. 5(a), we see that this occurs for $f_i = 0.01$ at $1/\bar{a}_R \approx 0.05$. If this onset occurs in the experiments at smaller $1/\bar{a}_R$ than in the simulations, the rise in \tilde{T} as $1/\bar{a}_R$ increases would be more gradual than the heuristic curve. Assumptions made in the way the programs calculate the probabilities of the various different outcomes of each electron-atom collision could give rise to such a difference [19]. For instance, the details of radiative cascades within the Rydberg ensemble are critically dependent on population remixing of different n, ℓ states due to electron-Rydberg collisions, and how each of these states decays radiatively [45].

We conclude from this analysis that the observed behavior of \tilde{T} versus $1/\bar{a}_R$ shown in Figs. 3 and 4 for $n > 40$ (roughly, $1/\bar{a}_R > 0.03$) is determined by ionizing electron-Rydberg collisions and is consistent with energy conservation as the plasma evolves. For $f_f \lesssim 0.5$, approximately 60% of the initial Rydberg binding energy is converted to ion kinetic energy. Above $f_f = 0.5$, a regime approached in our experiments and simulations only for $n \geq 80$, the initial ionization mechanisms which seed the plasma lead to low $T_{e,i}$ plasmas which expand slowly, but which ultimately ionize as much as $\gtrsim 80\%$ of the atoms. To conserve energy, the remaining Rydberg atoms are scattered to

more deeply bound states, leading to the significant increase in β above $f_f = 0.5$. This leads to the final ion kinetic energy increasing as a fraction of the initial Rydberg binding energy (i.e., an increase in \tilde{T}), since the energy released when a Rydberg atom is deexcited is proportional to its binding energy [19].

With regard to the Coulomb coupling parameter for the electrons, Γ_e , using Eq. (7) and $\tilde{T} = 0.6$ gives $\Gamma_e = 1.6/\tilde{a}_e$. This coupling reaches its maximum value of $\Gamma_e \approx 0.1$ near $1/\tilde{a}_e \approx 1/\tilde{a}_R = 0.07$. However, at larger values of $1/\tilde{a}_R$, \tilde{T} increases because the ionization fraction becomes large as described above, and Γ_e decreases to ≈ 0.05 for the highest Rydberg states we looked at, $n = 120$. Interestingly, this behavior is also well described using the threshold lowering (TL) picture [4,46]. In this regime, the atom cores are close enough such that $a_R \sim 2n^{*2}a_0$, and the atom potential wells overlap. This lowers the ionization threshold by an amount $\Delta = 2C_P \times e^2/4\pi\epsilon_0 a_R$ (in SI units), where C_P is a constant found to be $C_P = 11 \pm 5$ using a self-consistent calculation which accounts for the three-dimensional distribution of atom and ion cores. In this picture, if the Rydberg state lies within an energy Δ of the isolated-atom ionization limit, laser excitation actually creates a free electron with temperature $T_{e,0}$ such that $\Delta = |E_{b,i}| + \frac{3}{2}k_B T_{e,0}$. The TL condition is thus $\tilde{T} = \frac{2}{3}(\frac{2C_P}{\tilde{a}_R} - 1)$, and this prediction for \tilde{T} is shown in Fig. 4(d).

E. Results for $n \lesssim 40$

The numerical modeling approach also gives some insight into the evolution of Rydberg plasmas with $n \lesssim 40$. The results shown in Figs. 4(b) and 4(c) for $1/\tilde{a}_R < 0.02$ show quite good agreement with the experimental data in Fig. 3. There is significant scatter in the experimental results, filling nearly the entire range between the lines corresponding to $\Gamma_e = 0.02$ to 0.05, and the results of the numerical simulation are also in this range. However, closer inspection of Figs. 4(b) and 4(c) shows that there is a small but distinct systematic trend in the \tilde{T} values. Specifically, for $T_{e,i} = 50$ K, the \tilde{T} values are systematically higher than for $T_{e,i} = 5, 10$, and 25 K, for which the \tilde{T} values are reasonably consistent. As can be seen in Fig. 5(a), the difference between the $T_{e,i} = 50$ K and the 5, 10, and 25 K simulations is that the f_f values are significantly higher for 50 K than for the other temperatures. Indeed, for 5, 10, and 25 K, the final ionization fraction is almost equal to the initial value used in the simulations, $f_f \approx f_i$. In this parameter range, the avalanche is not a period when there is significant additional ionization. However, there is still significant exchange of energy between the plasma and the atoms during this period with the net result that the electrons are heated and the Rydberg atoms are deexcited.

The behavior of the $T_{e,i} = 10$ and 25 K results is to be expected in the regime where $n \lesssim 40$. Basically, the initial electrons are too cool to ionize the parent Rydberg atoms because $|E_{b,i}| > 4k_B T_{e,i}$. The $T_{e,i} = 50$ K simulations are the closest to the $\tilde{T} = 0.6$ line [i.e., the prediction of Eq. (12) as $f_f \rightarrow 0$], and this supports this argument that the initial 50 K electrons can cause enough ionization that the UNP evolution loosely approximates to the mechanism described in Sec. IV D, but for the lower $T_{e,i}$ electrons, this model is not valid. The fact that the experimental data in Fig. 3 parallel the simulations in Fig. 4 for $n \lesssim 40$ ($1/\tilde{a}_R < 0.02$) for $T_{e,i} = 10$ and 25 K

implies that, whatever the initial ionization mechanism in the experiments, it cannot produce electrons hot enough to cause ionization for samples with $n \lesssim 40$. The phenomenon is likely related to the decrease in ionization rates for all three plasma seeding processes as n decreases, as well as the fact that the number of ions needed to reach threshold for plasma formation and the ion potential well depth are proportional to each other. In other words, low ionization rates means fewer ions, which produces a potential well that can only trap electrons which are too cool to ionize the parent atoms.

Both the simulations in Fig. 4 for low $T_{e,i}$, and the experimental results in Fig. 3, show that the interaction between the plasma and cold Rydberg samples with $n \lesssim 40$ results in UNPs which evolve at constant Γ_e . However, the Γ_e values for such plasmas are significantly smaller than we see at higher n . Specifically, the data in Figs. 4(b) and 4(c) ($f_i = 0.01$ and 0.1, respectively) fall approximately on the line $\Gamma_e = 0.03$. However, the lines in Fig. 4 are drawn assuming that $\tilde{a}_e = \tilde{a}_R$. Using $\tilde{a}_e = \tilde{a}_R/f_f^{1/3}$ and $f_f = f_i$, the actual value is $\Gamma_e \approx 0.01$ for $1/\tilde{a}_R < 0.01$. In UNPs created by photoionization, evolution at constant Γ_e occurs due to competition between two limiting behaviors [8]. First, in the absence of TBR, adiabatic expansion cools the electrons faster than the rate at which a_e increases, and this would cause Γ_e to increase with time. On the other hand, TBR both increases T_e and reduces the electron density, thus increasing a_R , both of which would decrease Γ_e . For sufficiently high electron density and low electron temperatures, the balance between these two behaviors equilibrates the UNP to $\Gamma_e \sim 0.1$.

For UNPs evolving from Rydberg atoms with $n \lesssim 40$ in which the electrons are too cold to cause ionization, the TBR heating mechanism is replaced with Rydberg deexcitation collisions, which become more probable than exciting collisions below the bottleneck energy. While the TBR rate is proportional to $\rho_e^2 T_e^{-9/2}$, the Rydberg deexcitation rate is proportional to $\rho_e T_e^{-0.17}$ [19,41]. The deexcitation rate clearly has much weaker dependence on electron density and temperature than TBR, and additionally does not increase a_e . Based on this argument, deexcitation collisions have a weaker ability than TBR to heat the UNP and decrease Γ_e . On the other hand, some of this effect is offset by the fact that the amount by which deexcitation collisions heat the electrons is proportional to $|E_b|$ [19], and this is typically much greater in our situation for Rydberg plasmas with $n \lesssim 40$ than in photoionization-initiated UNPs where each TBR collision heats the plasma by an amount $\sim k_B T_e$. The heating provided by deexcitation collisions in this limit is sufficient to counterbalance the tendency for Γ_e to increase due to adiabatic expansion, but the plasmas are limited to $\Gamma_e \sim 0.01$ because the initial ionization mechanisms cannot provide a high enough electron density for $\Gamma_e \sim 0.1$ to be reached with the typical Rydberg densities used in our experiments.

The concept of avalanche ionization of Rydberg atoms by the UNP is not appropriate for Rydberg UNPs from atoms with $n \lesssim 40$ since no significant additional ionization happens after the plasma reaches threshold. In this regime, the “avalanche” is actually the time in which the plasma heats due to Rydberg deexcitation collisions, and this process does not have a well-defined end time. Rather, this electron heating mechanism gradually tapers off since the most of the Rydberg atoms

get left behind as the plasma expands. The only Rydberg atoms “carried along” as the plasma expands are those in the ionization-recombination cycle, just as in a photoionization-initiated UNP. This will be a much smaller number than the parent Rydberg ensemble since only a small fraction of this sample has ionized before the avalanche begins. Additionally, the stationary parent ensemble will undergo radiative decay at higher rates as the initial n decreases, further reducing its interaction with the UNP. For the nd states used in this work, the radiative lifetimes are $35\ \mu\text{s}$ at $n = 40$, but only $16\ \mu\text{s}$ at $n = 30$ [25]. Electron-Rydberg collisions will populate nearby high angular momentum states with much longer lifetimes, thereby mitigating some of this decline. However, there is not enough time for the few electrons (relative to the number of parent Rydberg atoms) to populate anything close to a statistical ensemble of ℓ states, which would have effective lifetimes in the $100\ \mu\text{s}$ to $1\ \text{ms}$ range for $n = 30\text{--}40$ [47]. We see the effect of the declining radiative lifetime at low n reflected in the number of atoms which end up in states with $n \leq 5$ at $40\ \mu\text{s}$ of evolution time: At $n = 40$ and above, this number is negligible, but for $n \leq 30$, the fraction in $n \leq 5$ states is typically at least 50%.

V. CONCLUSION

We have described an experimental and numerical study of the effective initial electron temperatures, $T_{e,0}$, in ultracold Rydberg plasmas. We find that, for plasmas which evolve

from Rydberg samples with $n > 40$ in the density range $10^7\text{--}10^9\ \text{cm}^{-3}$, the final ion kinetic energy, $(3/2)k_B T_{e,0}$, is related to the fraction of atoms which ionize. To maintain the energy balance, the remaining Rydberg atoms are much more deeply bound than the original state, and electron collisions with these atoms are more likely to heat the UNP than to cool it. In this regime, $T_{e,0}$ corresponds to between $0.6 \times |E_{b,f}|/k_B$ (for very low ionization fractions) and $2.5 \times |E_{b,f}|/k_B$ for the highest ionization level observed in our simulations, $f_f \approx 0.83$. Additionally, we find that $T_{e,0}$ is independent of the initial ionization mechanism which seeds the plasma. For cold Rydberg samples with $n \lesssim 40$, the initial ionization mechanisms which seed the plasma produce electrons which are too cold to cause further ionization. In this situation, the plasma evolves with constant, low, Γ_e values due to competition between adiabatic cooling and electron-Rydberg collisions which deexcite the atoms and heat the electrons.

ACKNOWLEDGMENTS

We are deeply indebted to F. Robicheaux for sharing his programs and advice on how to run them, as well as extensive conversations at all stages of this project. In addition, we acknowledge extensive discussions with T. F. Gallagher and C. W. S. Conover, as well as the loan of equipment from the former. This work has been supported by Colby College through the Division of Natural Sciences grants program, by Middlebury College, and by NSF (Grant No. 1068191).

-
- [1] T. C. Killian, S. Kulin, S. D. Bergeson, L. A. Orozco, C. Orzel, and S. L. Rolston, *Phys. Rev. Lett.* **83**, 4776 (1999).
 - [2] T. Killian, T. Pattard, T. Pohl, and J. Rost, *Phys. Rep.* **449**, 77 (2007).
 - [3] M. Lyon and S. L. Rolston, *Rep. Prog. Phys.* **80**, 017001 (2017).
 - [4] Y. Hahn, *Phys. Lett. A* **293**, 266 (2002).
 - [5] Y. C. Chen, C. E. Simien, S. Laha, P. Gupta, Y. N. Martinez, P. G. Mickelson, S. B. Nagel, and T. C. Killian, *Phys. Rev. Lett.* **93**, 265003 (2004).
 - [6] T. Wilson, W. T. Chen, and J. Roberts, *Phys. Plasmas* **20**, 073503 (2013).
 - [7] W.-T. Chen, C. Witte, and J. L. Roberts, *Phys. Rev. E* **96**, 013203 (2017).
 - [8] F. Robicheaux and J. D. Hanson, *Phys. Rev. Lett.* **88**, 055002 (2002).
 - [9] S. L. Rolston, S. D. Bergeson, S. Kulin, and C. Orzel, *Bull. Am. Phys. Soc.* **43**, 1324 (1998).
 - [10] M. P. Robinson, B. Laburthe Tolra, M. W. Noel, T. F. Gallagher, and P. Pillet, *Phys. Rev. Lett.* **85**, 4466 (2000).
 - [11] G. Vitrant, J. M. Raimond, M. Gross, and S. Haroche, *J. Phys. B* **15**, L49 (1982).
 - [12] J. P. Morrison, C. J. Rennick, J. S. Keller, and E. R. Grant, *Phys. Rev. Lett.* **101**, 205005 (2008).
 - [13] M. Schulz-Weiling, H. Sadeghi, J. Hung, and E. Grant, *J. Phys. B* **49**, 193001 (2016).
 - [14] P. J. Tanner, J. Han, E. S. Shuman, and T. F. Gallagher, *Phys. Rev. Lett.* **100**, 043002 (2008).
 - [15] F. Robicheaux, M. M. Goforth, and M. A. Phillips, *Phys. Rev. A* **90**, 022712 (2014).
 - [16] I. Beterov, D. Tretyakov, I. Ryabtsev, V. Entin, A. Ekers, and N. Bezuglov, *New J. Phys.* **11**, 013052 (2009).
 - [17] W. P. Spencer, A. G. Vaidyanathan, D. Kleppner, and T. W. Ducas, *Phys. Rev. A* **26**, 1490 (1982).
 - [18] W. Li, M. W. Noel, M. P. Robinson, P. J. Tanner, T. F. Gallagher, D. Comparat, B. Laburthe Tolra, N. Vanhaecke, T. Vogt, N. Zahzam, P. Pillet, and D. A. Tate, *Phys. Rev. A* **70**, 042713 (2004).
 - [19] F. Robicheaux and J. D. Hanson, *Phys. Plasmas* **10**, 2217 (2003).
 - [20] T. Pohl, T. Pattard, and J. M. Rost, *Phys. Rev. A* **68**, 010703(R) (2003).
 - [21] G. Bannasch, T. C. Killian, and T. Pohl, *Phys. Rev. Lett.* **110**, 253003 (2013).
 - [22] M. Robert-de-Saint-Vincent, C. S. Hofmann, H. Schempp, G. Günter, S. Whitlock, and M. Weidemüller, *Phys. Rev. Lett.* **110**, 045004 (2013).
 - [23] M. Siercke, F. E. Oon, A. Mohan, Z. W. Wang, M. J. Lim, and R. Dumke, *Phys. Rev. A* **89**, 022701 (2014).
 - [24] P. McQuillen, X. Zhang, T. Strickler, F. B. Dunning, and T. C. Killian, *Phys. Rev. A* **87**, 013407 (2013).
 - [25] D. B. Branden, T. Juhasz, T. Mahlokozera, C. Vesa, R. O. Wilson, M. Zheng, A. Kortyna, and D. A. Tate, *J. Phys. B* **43**, 015002 (2010).
 - [26] J. Han and T. F. Gallagher, *Phys. Rev. A* **79**, 053409 (2009).

- [27] N. Saquet, J. P. Morrison, M. Schulz-Weiling, H. Sadeghi, J. Yiu, C. J. Rennick, and E. R. Grant, *J. Phys. B* **44**, 184015 (2011).
- [28] K. A. Twedt, Ph.D. thesis, University of Maryland, College Park, MD, 2012, <https://drum.lib.umd.edu/handle/1903/12551>.
- [29] X. L. Zhang, R. S. Fletcher, S. L. Rolston, P. N. Guzdar, and M. Swisdak, *Phys. Rev. Lett.* **100**, 235002 (2008).
- [30] T. Pohl, T. Pattard, and J. M. Rost, *Phys. Rev. A* **70**, 033416 (2004).
- [31] D. Vrinceanu, *Phys. Rev. A* **72**, 022722 (2005).
- [32] T. C. Killian, M. J. Lim, S. Kulin, R. Dumke, S. D. Bergeson, and S. L. Rolston, *Phys. Rev. Lett.* **86**, 3759 (2001).
- [33] J. L. Roberts, C. D. Fertig, M. J. Lim, and S. L. Rolston, *Phys. Rev. Lett.* **92**, 253003 (2004).
- [34] R. S. Fletcher, X. L. Zhang, and S. L. Rolston, *Phys. Rev. Lett.* **99**, 145001 (2007).
- [35] P. Gupta, S. Laha, C. E. Simien, H. Gao, J. Castro, T. C. Killian, and T. Pohl, *Phys. Rev. Lett.* **99**, 075005 (2007).
- [36] J. P. Morrison, C. J. Rennick, and E. R. Grant, *Phys. Rev. A* **79**, 062706 (2009).
- [37] S. Kulin, T. C. Killian, S. D. Bergeson, and S. L. Rolston, *Phys. Rev. Lett.* **85**, 318 (2000).
- [38] F. Robicheaux, *J. Phys. B* **38**, S333 (2005).
- [39] I. I. Beterov, I. I. Ryabtsev, D. B. Tretyakov, and V. M. Entin, *Phys. Rev. A* **79**, 052504 (2009).
- [40] H. Sadeghi, A. Kruey, J. Hung, J. H. Gurian, J. P. Morrison, M. Schulz-Weiling, N. Saquet, C. J. Rennick, and E. R. Grant, *Phys. Rev. Lett.* **112**, 075001 (2014).
- [41] P. Mansbach and J. Keck, *Phys. Rev.* **181**, 275 (1969).
- [42] S. G. Kuzmin and T. M. O'Neil, *Phys. Plasmas* **9**, 3743 (2002).
- [43] T. Pohl, D. Vrinceanu, and H. R. Sadeghpour, *Phys. Rev. Lett.* **100**, 223201 (2008).
- [44] G. Bannasch and T. Pohl, *Phys. Rev. A* **84**, 052710 (2011).
- [45] F. Robicheaux (personal communication).
- [46] Y. Hahn, *Phys. Rev. E* **64**, 046409 (2001).
- [47] E. S. Chang, *Phys. Rev. A* **31**, 495 (1985).

Bibliography

- [1] D. L. Andrews and D. S. Bradshaw, *Laser cooling and trapping of atoms*, in Optical Nanomanipulation, 2053-2571, Morgan and Claypool Publishers, 2016, pp. 4–1 to 4–5.
- [2] F. F. Chen, *Introduction to Plasma Physics*, Springer, 1993.
- [3] E. V. Crockett, R. C. Newell, F. Robicheaux, and D. A. Tate, *Heating and cooling of electrons in an ultracold neutral plasma using Rydberg atoms*, Phys. Rev. A, 98 (2018), p. 043431.
- [4] G. T. Forest, Y. Li, E. D. Ward, A. L. Goodsell, and D. A. Tate, *Expansion of an ultracold Rydberg plasma*, Phys. Rev. A, 97 (2018), p. 043401.
- [5] S. Hamaguchi, R. T. Farouki, and D. H. E. Dubin, *Triple point of Yukawa systems*, Phys. Rev. E, 56 (1997), pp. 4671–4682.
- [6] T. C. Killian, *Ultracold neutral plasmas*, Science, 316 (2007), pp. 705–708.
- [7] T. C. Killian, S. Kulin, S. D. Bergeson, L. A. Orozco, C. Orzel, and S. L. Rolston, *Creation of an ultracold neutral plasma*, Phys. Rev. Lett., 83 (1999), pp. 4776–4779.
- [8] S. Kulin, T. C. Killian, S. D. Bergeson, and S. L. Rolston, *Plasma oscillations and expansion of an ultracold neutral plasma*, Phys. Rev. Lett., 85 (2000), pp. 318–321.
- [9] M. G. Littman, *Single-mode pulsed tunable dye laser*, Appl. Opt., 23 (1984), pp. 4465–4468.
- [10] A. Morozov, *Introduction to Plasma Dynamics*, CRC Press, 2012.
- [11] M. S. Murillo, *Using Fermi statistics to create strongly coupled ion plasmas in atom traps*, Phys. Rev. Lett., 87 (2001), p. 115003.
- [12] NobelPrize.org, *The nobel prize in physics 1997*, 2019.
- [13] R. Paschotta, *External-cavity diode lasers*, RP Photonics Encyclopedia, (2008).
- [14] T. Pohl, D. Comparat, N. Zahzam, T. Vogt, P. Pillet, and T. Pattard, *Use of Rydberg atoms to control electron temperatures in ultracold plasmas*, The European Physical Journal D, 40 (2006), p. 45–50.
- [15] N. Poudel, *Electronic detection of ultra cold neutral plasma*, Colby College Honors Thesis, (2012).
- [16] F. Robicheaux and J. D. Hanson, *Simulation of the expansion of an ultracold neutral*

- plasma*, Phys. Rev. Lett., 88 (2002), p. 055002.
- [17] F. Robicheaux and J. D. Hanson, *Simulated expansion of an ultra-cold, neutral plasma*, Physics of Plasmas, 10 (2003), p. 2217–2229.
- [18] S. Rolston, *Ultracold neutral plasmas*, Physics, 1 (2008).